

The first ultracompact Roche lobe–filling hot subdwarf binary

Thomas Kupfer, Evan B Bauer, Thomas R Marsh, Jan van Roestel, Eric C Bellm, Kevin B Burdge, Michael W Coughlin, Jim Fuller, J.J. Hermes, Lars Bildsten, Shrinivas R Kulkarni, Thomas A Prince, Paula Szkody, Vik S Dhillon, Gabriel Murawski, Rick Burruss, Richard Dekany, Alex Delacroix, Andrew J Drake, Dmitry A Duev, Michael Feeney, Matthew J Graham, David L Kaplan, Russ R Laher, S.P. Littlefair, Frank J Masci, Reed Riddle, Ben Rusholme, Eugene Serabyn, Roger M Smith, David L Shupe, Maayane T Soumagnac. "The First Ultracompact Roche Lobe–Filling Hot Subdwarf Binary." *The Astrophysical Journal*, Volume 891, Issue 1, pp. 45 - 45. <https://doi.org/10.3847/1538-4357/ab72ff>

<https://hdl.handle.net/2144/42245>

"Downloaded from OpenBU. Boston University's institutional repository."



The First Ultracompact Roche Lobe–Filling Hot Subdwarf Binary

Thomas Kupfer¹, Evan B. Bauer¹, Thomas R. Marsh², Jan van Roestel³, Eric C. Bellm⁴, Kevin B. Burdge³, Michael W. Coughlin³, Jim Fuller³, JJ Hermes⁵, Lars Bildsten^{1,6}, Shrinivas R. Kulkarni³, Thomas A. Prince³, Paula Szkody⁷, Vik S. Dhillon^{8,9}, Gabriel Murawski¹⁰, Rick Burruss¹¹, Richard Dekany¹¹, Alex Delacroix¹¹, Andrew J. Drake³, Dmitry A. Dhev³, Michael Feeney¹¹, Matthew J. Graham³, David L. Kaplan¹², Russ R. Laher¹³, S. P. Littlefair⁸, Frank J. Masci¹³, Reed Riddle¹¹, Ben Rusholme¹³, Eugene Serabyn¹⁴, Roger M. Smith¹¹, David L. Shupe¹³, and Maayane T. Soumagnac^{15,16}

¹ Kavli Institute for Theoretical Physics, University of California, Santa Barbara, CA 93106, USA; tkupfer@ucsb.edu

² Department of Physics, University of Warwick, Coventry CV4 7AL, UK

³ Division of Physics, Mathematics and Astronomy, California Institute of Technology, Pasadena, CA 91125, USA

⁴ DIRAC Institute, Department of Astronomy, University of Washington, 3910 15th Avenue NE, Seattle, WA 98195, USA

⁵ Department of Astronomy, Boston University, 725 Commonwealth Avenue, Boston, MA 02215, USA

⁶ Department of Physics, University of California, Santa Barbara, CA 93106, USA

⁷ University of Washington, Department of Astronomy, Box 351580, Seattle, WA 98195, USA

⁸ Department of Physics & Astronomy, University of Sheffield, Sheffield S3 7RH, UK

⁹ Instituto de Astrofísica de Canarias, Via Lactea s/n, La Laguna, E-38205 Tenerife, Spain

¹⁰ Gabriel Murawski Private Observatory (SOTES), Poland

¹¹ Caltech Optical Observatories, California Institute of Technology, Pasadena, CA 91125, USA

¹² Center for Gravitation, Cosmology and Astrophysics, Department of Physics, University of Wisconsin–Milwaukee, P.O. Box 413, Milwaukee, WI 53201, USA

¹³ IPAC, California Institute of Technology, 1200 East California Boulevard, Pasadena, CA 91125, USA

¹⁴ Jet Propulsion Laboratory, California Institute of Technology, Pasadena, CA 91109, USA

¹⁵ Lawrence Berkeley National Laboratory, 1 Cyclotron Road, Berkeley, CA 94720, USA

¹⁶ Department of Particle Physics and Astrophysics, Weizmann Institute of Science, Rehovot 76100, Israel

Received 2020 January 15; revised 2020 January 30; accepted 2020 February 3; published 2020 March 3

Abstract

We report the discovery of the first short-period binary in which a hot subdwarf star (sdOB) filled its Roche lobe and started mass transfer to its companion. The object was discovered as part of a dedicated high-cadence survey of the Galactic plane named the Zwicky Transient Facility and exhibits a period of $P = 39.3401(1)$ minutes, making it the most compact hot subdwarf binary currently known. Spectroscopic observations are consistent with an intermediate He-sdOB star with an effective temperature of $T_{\text{eff}} = 42,400 \pm 300$ K and a surface gravity of $\log(g) = 5.77 \pm 0.05$. A high signal-to-noise ratio GTC+HiPERCAM light curve is dominated by the ellipsoidal deformation of the sdOB star and an eclipse of the sdOB by an accretion disk. We infer a low-mass hot subdwarf donor with a mass $M_{\text{sdOB}} = 0.337 \pm 0.015 M_{\odot}$ and a white dwarf accretor with a mass $M_{\text{WD}} = 0.545 \pm 0.020 M_{\odot}$. Theoretical binary modeling indicates the hot subdwarf formed during a common envelope phase when a $2.5\text{--}2.8 M_{\odot}$ star lost its envelope when crossing the Hertzsprung gap. To match its current P_{orb} , T_{eff} , $\log(g)$, and masses, we estimate a post–common envelope period of $P_{\text{orb}} \approx 150$ minutes and find that the sdOB star is currently undergoing hydrogen shell burning. We estimate that the hot subdwarf will become a white dwarf with a thick helium layer of $\approx 0.1 M_{\odot}$, merge with its carbon/oxygen white dwarf companion after ≈ 17 Myr, and presumably explode as a thermonuclear supernova or form an R CrB star.

Unified Astronomy Thesaurus concepts: B subdwarf stars (129); Stellar evolution (1599); Compact binary stars (283); White dwarf stars (1799)

1. Introduction

Hot subdwarf B/O (sdB/O) stars are stars with spectral type B or O that are less luminous than main-sequence stars with the same spectral type. Most are thought to be compact He-burning stars with masses around $0.5 M_{\odot}$ and with thin hydrogen envelopes (Heber 1986, 2009, 2016). It has been shown that a large number of sdB stars are in close orbits with orbital periods of $P_{\text{orb}} < 10$ days (Napiwotzki et al. 2004; Maxted et al. 2001). The most compact systems have orbital periods of $\lesssim 1$ hr (e.g., Vennes et al. 2012; Geier et al. 2013; Kupfer et al. 2017a, 2017b). A possible mechanism that may form such tight binaries is orbital shrinkage through a common envelope phase, followed by the loss of angular momentum due to the radiation of gravitational waves (Han et al. 2002, 2003; Nelemans 2010).

Hot subdwarf binaries with white dwarf (WD) companions that exit the common envelope phase at $P_{\text{orb}} \lesssim 2$ hr will overflow their Roche lobes while the sdB is still burning

helium. Due to the emission of gravitational waves, the orbit of the binary will shrink until the sdB/O fills its Roche lobe at a period of $\approx 20\text{--}40$ minutes, depending on the evolutionary stage of the hot subdwarf (e.g., Savonije et al. 1986; Tutukov & Fedorova 1989; Tutukov & Yungelson 1990; Iben & Tutukov 1991; Yungelson 2008; Piersanti et al. 2014; Brooks et al. 2015). However, no hot subdwarf in a tight accreting binary that fills its Roche lobe has been found so far.

The known population of sdB binaries consists mostly of systems with orbital periods too large to initiate accretion before the sdB evolves into a WD (Kupfer et al. 2015). Currently, only three systems with a WD companion are known to have $P_{\text{orb}} < 2$ hr (Vennes et al. 2012; Geier et al. 2013; Kupfer et al. 2017a, 2017b).

Kupfer et al. (2017a) discovered the most compact binary consisting of a hot subdwarf star with a massive WD companion as part of the OmegaWhite survey (Macfarlane

et al. 2015; Toma et al. 2016; Macfarlane et al. 2017). The object OW J074106.0–294811.0 has a period of only 44 minutes. However, the analysis revealed that the hot subdwarf has a mass of only $0.23 \pm 0.12 M_{\odot}$ and is inconsistent with a canonical-mass helium-burning sdB star; instead, it is fully consistent with a helium core WD with a mass of $0.32 M_{\odot}$. If the hot subdwarf star is a helium WD, the system will start accretion at an orbital period of ≈ 5 minutes. Depending on the spin–orbit synchronization timescale, the object will either merge and form an R CrB star or end up as a stable accreting AM CVn-type system with an He WD donor (Kupfer et al. 2017a).

The most compact known sdB binary where the sdB is still undergoing helium core burning is CD $-30^{\circ}11223$. The binary has an orbital period $P_{\text{orb}} = 70.5$ minutes and a high-mass WD companion ($M_{\text{WD}} \approx 0.75 M_{\odot}$; Vennes et al. 2012; Geier et al. 2013). The sdB in CD $-30^{\circ}11223$ will overflow its Roche lobe in ≈ 40 million yr, when the system will have shrunk to an orbital period of $P_{\text{orb}} \approx 40$ minutes. The sdB will start accretion onto the WD companion, and after accreting $\approx 0.1 M_{\odot}$, helium burning is predicted to be ignited unstably in the accreted helium layer on the surface of the WD (Brooks et al. 2015; Bauer et al. 2017). This could either disrupt the WD even if the mass is significantly below the Chandrasekhar mass, a so-called double detonation SN Ia (e.g., Livne 1990; Livne & Arnett 1995; Fink et al. 2010; Woosley & Kasen 2011; Wang & Han 2012; Shen & Bildsten 2014; Wang 2018) or just detonate the He shell without disrupting the WD; the latter scenario results in a faint and fast SN Ia with subsequent weaker He flashes (Bildsten et al. 2007; Brooks et al. 2015). Therefore, systems like CD $-30^{\circ}11223$ are predicted to be either the progenitors for double detonation SNe Ia or perhaps faint and fast SNe Ia when the WD is not disrupted. If the WD explodes, the companion will move translationally with the original orbital velocity, and US 708 is a candidate that is proposed to be the former donor star in such a binary system (Geier et al. 2015).

Sub-Chandrasekhar mass SN Ia explosions with thick helium shells accreted from a helium-rich companion are predicted to exhibit an early-time flux excess and red colors (Polin et al. 2019). De et al. (2019) discovered a SN Ia that matches all of the properties predicted for a double detonation SN Ia with a massive helium shell and pre-explosion properties similar to CD $-30^{\circ}11223$.

Although a clean picture has evolved with evidence for systems that will start accretion before the hot subdwarf has evolved into a WD, no accreting WD with a Roche lobe–filling hot subdwarf donor has yet been found. The only known hot subdwarf binary showing signs of accretion is HD 49798, which consists of a massive sdO primary with a massive compact companion in a 1.55 day orbit (Thackeray 1970; Dufton 1972; Kudritzki & Simon 1978). Israel et al. (1995, 1997) reported X-ray pulses with a period of 13.2 s, which was interpreted as the spin period of a magnetic compact companion accreting from the sdO wind. Mereghetti et al. (2009) detected an eclipse in the X-ray light curve with a period coincident with the spectroscopic period, allowing them to derive precise masses of the sdO ($M_{\text{sdO}} = 1.50 \pm 0.05 M_{\odot}$) and its compact companion ($M = 1.28 \pm 0.05 M_{\odot}$). Follow-up studies could not fully resolve the nature of the compact companion (Mereghetti et al. 2009, 2011, 2013; Mereghetti & La Palombara 2016). Brooks et al. (2017) showed that the

massive sdO in HD 49798 will fill its Roche lobe in ≈ 65 kyr and start accretion onto its compact companion with a rate of $\approx 10^{-5} M_{\odot} \text{ yr}^{-1}$.

Here we present the discovery of the most compact sdOB binary, ZTF J213056.71+442046.5 (hereafter ZTF J2130+4420), that matches the properties of a hot subdwarf star that fills its Roche lobe and has started mass transfer to the WD companion. We discovered the object (but did not announce our finding) in fall 2018 in a search for periodic objects in the hot subdwarf catalog of $\approx 40,000$ hot subdwarf candidates presented in Geier et al. (2019) using data from our dedicated high-cadence survey at low Galactic latitudes as part of the Zwicky Transient Facility (ZTF). Independently, on 2019 May 25, Gabriel Murawski reported the object to the International Variable Star Index (VSX)¹⁷ and in two Astronomer’s Telegrams, Rivera Sandoval et al. (2019) reported the absence of X-ray emission from 1 ks *Swift* observations, and Ramsay et al. (2019) reported spectroscopic observations suggesting an He-sdOB star classification for ZTF J2130+4420.

2. Observations

As part of the ZTF, the Palomar 48 inch (P48) telescope images the sky every clear night (Bellm et al. 2019b; Graham et al. 2019). The binary ZTF J2130+4420 was first discovered in a dedicated high-cadence survey at low Galactic latitudes performed in the ZTF *r* band (Bellm et al. 2019a). The high-cadence data were complemented by data from the ZTF public survey obtained in 2018 that were made available after data release 1 on 2018 May 8. The ZTF light curves of ZTF J2130+4420 consist of 759 epochs in the ZTF *r* band and 175 epochs in the ZTF *g* band. Image processing and light-curve extraction of ZTF data are described in detail by Masci et al. (2019).

High-cadence follow-up observations with 1 and 2 s exposure time were conducted using the Kitt Peak 84 inch Electron Multiplying Demonstrator (KPED; Coughlin et al. 2019), which is a photometer that uses a frame-transfer EMCCD to achieve 15 ms dead time covering a 4.4×4.4 field of view. Data reduction was carried out with a customized pipeline. All frames were bias-subtracted and flat-fielded.

Additionally, ZTF J2130+4420 was observed with HiPERCAM, a five-beam imager equipped with frame-transfer CCDs allowing the simultaneous acquisition of u_s -, g_s -, r_s -, i_s -, and z_s -band images at a rate of up to 1000 frames s^{-1} (Dhillon et al. 2016, 2018). For these data, HiPERCAM was mounted on the 10.4 m Gran Telescopio Canarias (GTC) on the island of La Palma in Spain. On the night of 2019 July 7, ZTF J2130+4420 was observed at 1.766 s cadence with a dead time of 10 ms for 1576 frames with HiPERCAM in a run lasting 46 minutes, covering a little more than one 39 minute binary orbit; the cadence in u_s alone was a factor of 2 slower than the other four bands to optimize the signal-to-noise ratio (S/N). The sky was clear with $0''.8$ – $1''.5$ seeing. The data were reduced using the dedicated HiPERCAM pipeline,¹⁹ including debiasing and flat-fielding. Differential photometry was performed.

Phase-resolved spectroscopy of ZTF J2130+4420 was obtained using the Keck I telescope and the blue arm of the Low Resolution Imaging Spectrometer (LRIS; McCarthy et al.

¹⁷ <https://www.aavso.org/vsx/index.php?view=detail.top&oid=689728>

¹⁸ HiPERCAM uses high-throughput versions of the SDSS filters known as Super-SDSS filters, and we denote these filters u_s , g_s , r_s , etc.

¹⁹ <https://github.com/HiPERCAM/>

Table 1
Summary of the Observations

Date	UT	Tele./Inst.	N_{exp}	Exp. Time (s)	Coverage (Å)/Filter
Photometry					
2018 Apr 10–2018 Nov 21		P48	759	30	ZTF <i>r</i>
2018 Mar 31–2018 Nov 9		P48	175	30	ZTF <i>g</i>
2019 Apr 28	10:56–11:45	84 inch/KPED	1452	2	<i>g'</i>
2019 May 1	10:33–11:49	84 inch/KPED	2270	2	<i>g'</i>
2019 May 14	09:29–10:29	84 inch/KPED	2950	1	<i>g'</i>
2019 May 28	09:30–11:30	84 inch/KPED	3585	2	<i>g'</i>
2019 Jul 8	04:04–04:51	GTC/HiPERCAM	789/1577	3.54/1.77	$u_s/g_s, r_s, i_s, z_s$
Spectroscopy					
2019 Jan 27	04:54–05:22	Keck/LRIS	14	60	3200–5300
2019 May 30	09:09–09:44	200 inch/DBSP	8	240	3500–10 500
2019 Jun 25	01:30–05:37	WHT/ISIS	105	120	3100–5300 and 6350–8100
2019 Jun 26	02:12–05:26	WHT/ISIS	86	120	3100–5300 and 6350–8100

1998) using a low-resolution mode ($R \approx 1400$). We obtained a total of 14 spectra. Data reduction was performed with the Lpipe pipeline²⁰ (Perley 2019).

Optical spectra were also obtained with the Palomar 200 inch telescope and the Double Spectrograph (DBSP; Oke & Gunn 1982) using a low-resolution mode ($R \approx 1200$). Both arms of the spectrograph were reduced using a custom PyRAF-based pipeline²¹ (Bellm & Sesar 2016). The pipeline performs standard image processing and spectral reduction procedures, including bias subtraction, flat-field correction, wavelength calibration, optimal spectral extraction, and flux calibration.

Additionally, ZTF J2130+4420 was observed with the 4.2 m William Herschel Telescope (WHT) and the ISIS spectrograph (Carter et al. 1993) using a low-/medium-resolution mode (R300B and R600R grating, $R \approx 1500$ and 3500). Ten bias frames were obtained to construct an average bias frame, and 10 individual lamp flat fields were obtained to construct a normalized flat field. One-dimensional spectra were extracted using optimal extraction and subsequently wavelength- and flux-calibrated. An arc lamp spectrum was taken at the position of the target before and after each observing sequence for LRIS, DBSP, and ISIS, as well as after every hour for ISIS to account for telescope flexure.

All times in each data set were converted to the barycentric dynamical timescale, corrected to the solar system barycenter, MJD(BTDB). Table 1 gives an overview of all observations and the instrumental setups.

3. Orbital and Atmospheric Parameters

The object ZTF J2130+4420 shows strong periodic variability in its light curves (Figure 1). This variability is primarily caused by the tidal deformation of the sdOB primary under the influence of the gravitational force of the companion. We use the ZTF light curve with its multimonth baseline in combination with the KPED light curves and the HiPERCAM light curve to derive the orbital period of the system. The analysis was done with the Gatspy (Vanderplas 2015; Vanderplas & Ivezić 2015) module for time series analysis, which uses the Lomb–Scargle periodogram (Scargle 1982). We find an orbital period of $P = 39.3401(1)$ minutes. The uncertainty was derived from a bootstrapping analysis. To

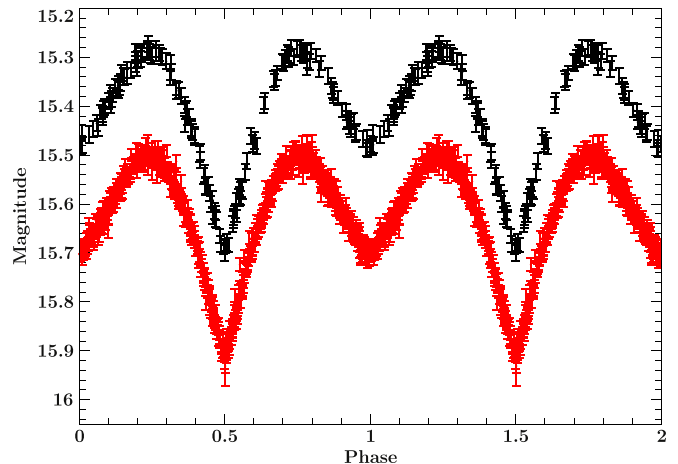


Figure 1. Phase-folded ZTF *g* (black) and *r* (red) discovery light curves.

determine the ephemeris, we measured the deepest point in the light curve, corresponding to the phase when the sdOB is furthest away from the observer. We used the parameter from the best model derived in Section 4 and only fit the zero-point of the ephemeris (T_0) to the HiPERCAM and KPED light curves. We find an ephemeris of

$$T_0(\text{BMJD}) = 58672.18085(78) + 0.0273195(2)E, \quad (1)$$

where E corresponds to the epoch.

The overall spectrum of ZTF J2130+4420 shows Balmer lines, as well as neutral (He I) and ionized (He II) helium lines (Figure 2); it can be well fit with a single He-sdOB star. We do not find evidence for a companion or accretion disk in the overall spectrum. The atmospheric parameters of effective temperature, T_{eff} ; surface gravity, $\log(g)$, and helium abundance, $\log y$, where $y = n(\text{He})/n(\text{H})$; and projected rotational velocity, $v_{\text{rot}} \sin i$, were determined for the sdOB by fitting the rest wavelength-corrected average LRIS, DBSP, and WHT spectra with metal-free NLTE model spectra (Stroeer et al. 2007). The ionization equilibrium between the He I and He II is most sensitive to the effective temperature of the sdOB, whereas the broad hydrogen lines in the blue are most sensitive to $\log g$. The full procedure is described in detail in Kupfer et al. (2017a, 2017b). The best fit was derived using a χ^2 minimization for each spectrum. We adopted the weighted mean of T_{eff} , $\log(g)$, $\log y$, and $v_{\text{rot}} \sin i$ as the final solution. We find $T_{\text{eff}} = 42,400 \pm 300$ K, $\log(g) = 5.77 \pm 0.05$, and

²⁰ <http://www.astro.caltech.edu/~dperley/programs/lpipe.html>

²¹ <https://github.com/ebellm/pyraf-dbsp>

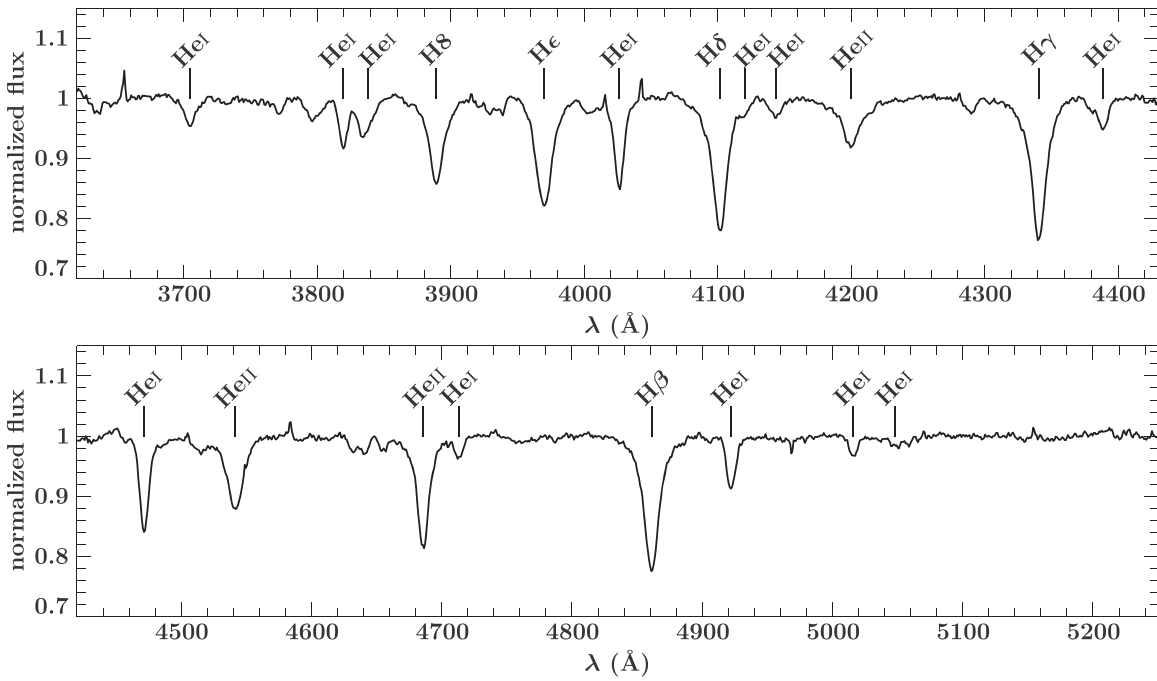


Figure 2. Normalized average WHT spectrum of ZTF J2130+4420. All prominent lines are marked.

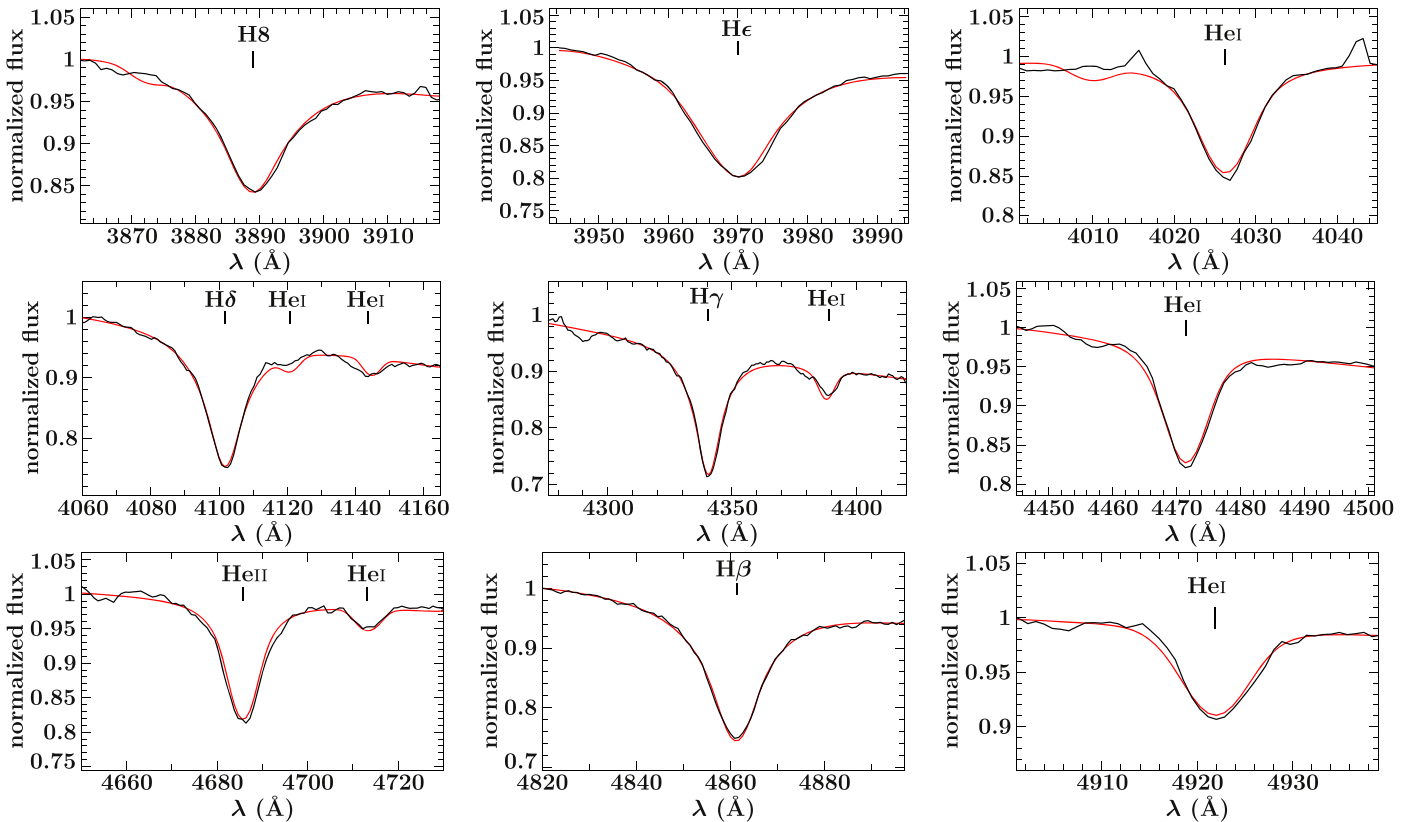


Figure 3. Fit of synthetic NLTE models to the hydrogen Balmer, as well as neutral and ionized helium lines of the coadded WHT spectrum. The black solid line corresponds to the spectrum, and the red solid line corresponds to the fit.

$\log y = -0.52 \pm 0.03$. Figure 3 shows the fit to the WHT spectrum, and Table 2 summarizes the results from the spectroscopic fits to the average LRIS, DBSP, and WHT spectra. The occurrence of both He I and He II, as well as the increased helium abundance $\log y > -1$, classifies the hot subdwarf as an intermediate He-sdOB (see Heber 2016).

To measure radial velocities (RVs), we folded the individual WHT/ISIS spectra on the ephemeris shown in Equation (1) into 20 phase bins and coadded individual spectra observed at the same binary phase. This leads to an S/N per phase bin of ≈ 100 , well suited to measure velocities with a precision of $\approx 5 \text{ km s}^{-1}$. The RVs were measured by fitting Gaussians,

Table 2
Summary of Atmospheric Parameter ZTF J2130+4420

Instrument	T_{eff} (K)	$\log(g)$	$\log y$	$v_{\text{rot}} \sin i$ (km s^{-1})
LRIS	$42,400 \pm 500$	5.78 ± 0.08	-0.48 ± 0.06	246 ± 28
DBSP	$42,100 \pm 600$	5.82 ± 0.07	-0.56 ± 0.06	238 ± 25
ISIS	$42,500 \pm 400$	5.72 ± 0.06	-0.52 ± 0.04	234 ± 21
Adopted	$42,400 \pm 300$	5.77 ± 0.05	-0.52 ± 0.03	238 ± 15

Lorentzians, and polynomials to the hydrogen and helium lines to cover the continuum, line, and line core of the individual lines using the FITSB2 routine (Napiwotzki et al. 2004). The procedure is described in full detail in Geier et al. (2011). We fit the wavelength shifts compared to the rest wavelengths using a χ^2 minimization. Assuming circular orbits, a sine curve was fit to the folded RV data points (Figure 4), excluding the data points around phases 0.8–1 and 0–0.2. We find a velocity semi-amplitude $K = 418.5 \pm 2.5 \text{ km s}^{-1}$. Around phase 0 (or 1), when the sdOB is furthest away from the observer, the velocity curve deviates significantly from a pure sine curve, which can be explained with the Rossiter–McLaughlin effect when the rapidly rotating sdOB is eclipsed by the accretion disk. The red curve in Figure 4 shows the residuals predicted from the Rossiter–McLaughlin effect calculated from our best-fitting model (see Section 4). To do so, we assumed that the equivalent widths of the photospheric lines were constant at points over the sdOB, so that the absolute flux in the lines simply varies with the local surface brightness. Parts of the star blocked by the accretion disk were ignored when computing line profiles.

4. Light-curve Modeling

The LCURVE code was used to perform the light-curve analysis (Copperwheat et al. 2010). The code uses grids of points to model the two stars. The shape of the stars in the binary is set by a Roche potential. We assume that the orbit is circular and the rotation periods of the stars are synchronized to the orbital period. The flux that each point on the grid emits is calculated by assuming a blackbody of a certain temperature at the bandpass wavelength, corrected for limb darkening, gravity darkening, Doppler beaming, and the reflection effect. In what follows, orbital phase zero is the conjunction phase when the sdOB is furthest away from Earth and being eclipsed by the accretion disk. Additionally, we fix the orbital period to the value determined in Section 3, as well as the effective temperature (T_{eff}), RV amplitude (K), and surface gravity (g) of the sdOB star (see Section 3).

The light curve of ZTF J2130+4420 is dominated by ellipsoidal modulations due to tidal distortion of the sdOB. Ellipsoidal modulations are sensitive to the mass ratio, the size of the distorted star relative to the orbital separation, and the limb and gravity darkening (Morris 1985). We set the latter parameters according to the tables of Claret & Bloemen (2011) shown in Table 3. We initially tried to model the light curve assuming that the system was composed of two detached stars, although we allowed the sdOB star to fill its Roche lobe if need be. It was quickly apparent that this model was inadequate, as it shows large residuals around orbital phases 0 and 0.5 (left panel of Figure 5). A value of $\chi^2 \approx 40,000$ was obtained for just 1576 data points, an extremely poor fit.

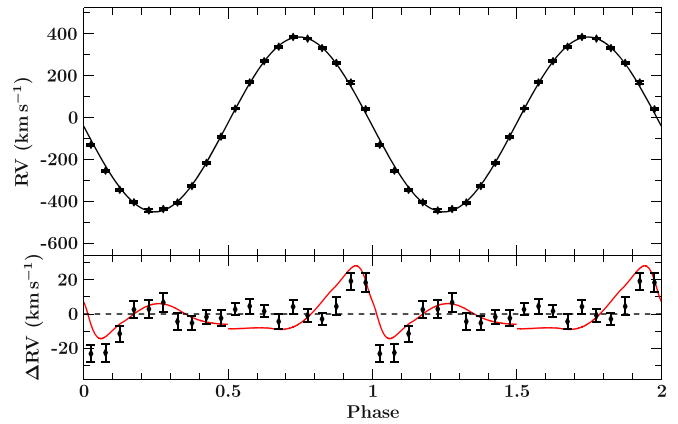


Figure 4. Measured RV vs. orbital phase for ZTF J2130+4420. The RV data were phase-folded with the orbital period and are plotted twice for better visualization. The residuals are plotted below. The strong deviation from a pure sine curve around phase 0 (1) can be explained by the Rossiter–McLaughlin effect occurring when the accretion disk eclipses the rapidly rotating sdOB. The red curve shows the predicted residuals for the Rossiter–McLaughlin effect from our best-fitting model (see Section 4). The RVs were measured from spectra obtained with WHT/ISIS.

Table 3
Overview of the Fixed Parameters for the LCURVE Fit to the HiPERCAM Light Curve for ZTF J2130+4420

Parameter	u_s	g_s	r_s	i_s	z_s
Beaming factor (F)	1.55	1.40	1.30	1.24	1.20
Gravity darkening β	0.34	0.28	0.27	0.26	0.26
Limb darkening a_1	1.20	1.22	1.17	1.10	1.12
Limb darkening a_2	-1.74	-1.82	-1.89	-1.82	-1.82
Limb darkening a_3	1.56	1.62	1.70	1.64	1.72
Limb darkening a_4	-0.54	-0.55	-0.57	-0.56	-0.60

The two-star model particularly fails around the phase when the sdOB is furthest from us. The light curve at this point shows a sharp and deep minimum that two stars alone cannot match. This is despite the sdOB star in our models expanding to fill $>99\%$ of its Roche lobe and thus maximizing the ellipsoidal modulations produced. The models were obtained through Markov Chain Monte Carlo (MCMC) iteration, a highly robust form of optimization, since it is easy to ignore nonphysical models such as overflowing of the Roche lobe. The only way the two-star model can even approach the data is to add a transit of the sdOB’s companion star across the face of the sdOB to deepen the minimum at phase 0, which leads to a strong constraint upon the size of the companion star, as it must block $\approx 10\%$ of the light from the sdOB. At phase 0.5, the eclipse of the companion star, along with the radius constraint from phase 0, fixes the temperature of the companion. The resulting radius and temperature for the companion can be ruled out on astrophysical grounds, compounding the poor fit delivered by the two-star model. The mass function from the RV curve of the sdOB implies an absolute minimum mass for the companion of $0.22 M_{\odot}$ (for a zero-mass sdOB) and a more realistic minimum of $0.5 M_{\odot}$ if one assumes that $M_{\text{sdOB}} \geq 0.25 M_{\odot}$. The companion must therefore be a compact remnant, almost certainly a WD, as no other stars of this mass can fit within their Roche lobes at an orbital period of 39 minutes. However, the radius found for the companion is roughly four times larger than a WD of this mass, and its temperature is an implausibly low $\approx 2000 \text{ K}$. In summary, a simple two-star

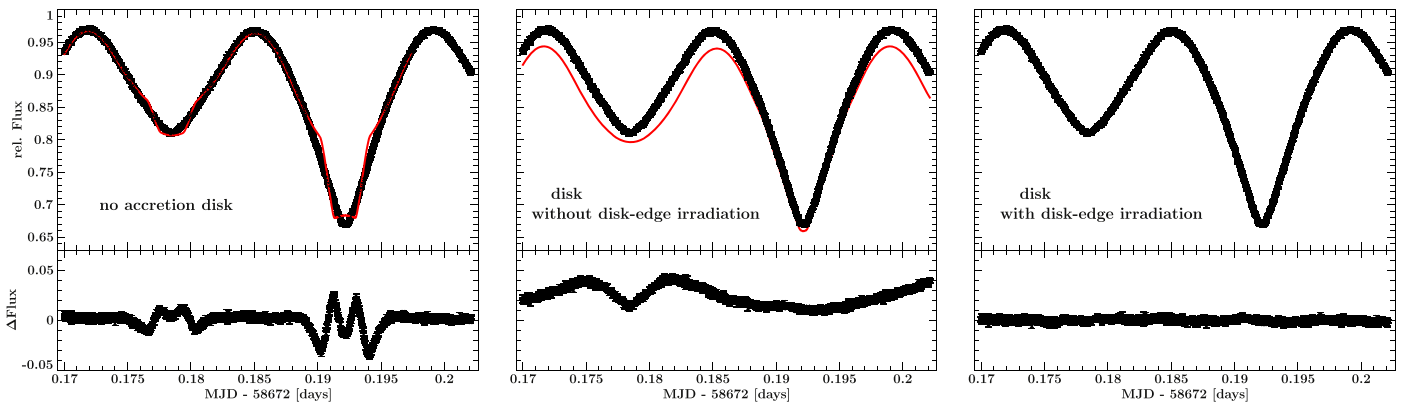


Figure 5. The left panel shows the best fit (red curve) to the g_s -band HiPERCAM data (black points) using just two stars. The middle panel shows the fit without the flux from the irradiated rim of the disk facing the sdOB star. The right panel shows the same fit when a disk and an irradiated rim of the disk facing the sdOB star are added. The residuals are shown below.

model cannot fit ZTF J2130+4420. We found the problem of the oversized radius to be highly robust. Even allowing the limb- and gravity-darkening coefficients to float free (and iterate toward implausible values), the radius of the sdOB’s companion remained far too large for a WD of its mass.

The deep minimum at phase 0 points toward obscuration by some other structure. The compact nature of the binary and the tendency for the sdOB to fill its Roche lobe in the two-star model clearly suggest that we may be seeing occultation by an accretion disk associated with mass transfer. We therefore considered a model with two stars and an accretion disk. The LCURVE code allows for axisymmetric disks with a height and temperature that vary with radius and inner and outer radii. This immediately led to a much better fit, but one that was still some way off from the data with $\chi^2 \approx 15,000$ for just 1576 data points. The main discrepancy was that the orbital phases of maximum flux in the data were closer to phase 0.5 when the sdOB was closest to us than the model seemed to be able to achieve. We then realized that if there is a disk in ZTF J2130+4420, it must be a highly unusual one in that it is strongly irradiated by the donor star. This is, for example, in contrast to cataclysmic variable stars, which have low luminosity, low-mass main-sequence donor stars, and compact object X-ray binaries that are strongly irradiated but from sources located at the center of their disks. The configuration of ZTF J2130+4420 means that the surface of the disk will be irradiated, quite possibly by more flux than is generated through accretion, and, moreover, the rim of the disk that is closest to the sdOB star will be particularly strongly irradiated. We therefore added a disk edge component in the form of a squat cylinder of radius and height equal to that at the outer radius of the accretion disk. We allowed this edge to have a fixed temperature supplemented by irradiation determined by flux balancing according to the level of irradiating flux each element receives from the sdOB star, modeled as a point source. The edge component is particularly hot (around 30,000 K) on the side of the disk closest to the sdOB and hottest at the point where the disk edge crosses the line of centers between the two stars. This leads to a sinusoidal modulation of flux that peaks at phase 0.5 (ignoring the possibility of eclipse for the moment), bringing the phases of maximum flux closer to 0.5 as observed.

The irradiated disk edge model is shown in the right panel of Figure 5. The value of χ^2 for this model was around 2000 for 1576 points, resulting in a reduced $\chi^2 \approx 1.3$, which is a considerable improvement over each of the other two models

discussed. While there are still some residuals, they do not have the symmetry of the main light curve and presumably reflect variations in the geometry of the disk not captured in our model. We are more surprised by how small these residuals are than by their presence; there is, for instance, no obvious sign of a contribution from a “bright spot” where the mass transfer stream hits the disk. Finally, in the middle panel of Figure 5, we show the identical model but with the flux from the disk edge turned off to show its significance and how it improves the agreement between the phases of maximum flux in the model compared to the data; in this case, we do account for the eclipse of the disk edge by the sdOB.

For the final model, we normalized the errors in the data to account for the small additional residuals and obtain a reduced $\chi^2 \approx 1$. We assume a Roche lobe-filling sdOB star, an irradiated disk, and an accreting WD. The passband-specific beaming parameter B ($F_\lambda = F_{0,\lambda}[1 - B_c^{\frac{1}{c}}]$; see Bloemen et al. 2011) was calculated following the approximation from Loeb & Gaudi (2003). The passband-specific gravity and limb darkening was taken from Claret & Bloemen (2011) for a $T_{\text{eff}} = 42,500$ K and $\log(g) = 5$ star, as higher $\log(g)$ values are not available. We investigated how the gravity-darkening (β) and limb-darkening (a_1, a_2, a_3, a_4) coefficients affect the results by adding them as free parameters with Gaussians around the theoretical value with FWHMs of $\sigma_\beta = 0.03$, $\sigma_{a_1} = 0.05$, and $\sigma_{a_2} = 0.05$. The variables a_3 and a_4 were not varied. The covariance between the gravity- and limb-darkening parameters and system parameters is negligible compared to the uncertainty on the parameters. Therefore, we kept the limb- and gravity-darkening coefficients fixed to the theoretical values from Claret & Bloemen (2011). The values used for the beaming, limb darkening, and gravity darkening are shown in Table 3. We did not use any limb or gravity darkening in the WD model, since these do not affect the light curve. This leaves as free parameters in the model the mass ratio q , inclination i , WD temperature T_{WD} , scaled radius of the WD companion r_{WD} , velocity scale ($[K + K_{\text{WD}}]/\sin i$), scaled disk size, disk height, and disk temperature, as well as the disk edge temperature and a bandpass-dependent disk edge reflection coefficient. Besides these system parameters, we added a first-order polynomial to correct for any residual airmass effects.

To determine the uncertainties in the parameters, we combine LCURVE with emcee (Foreman-Mackey et al. 2013), an implementation of an MCMC sampler that uses a

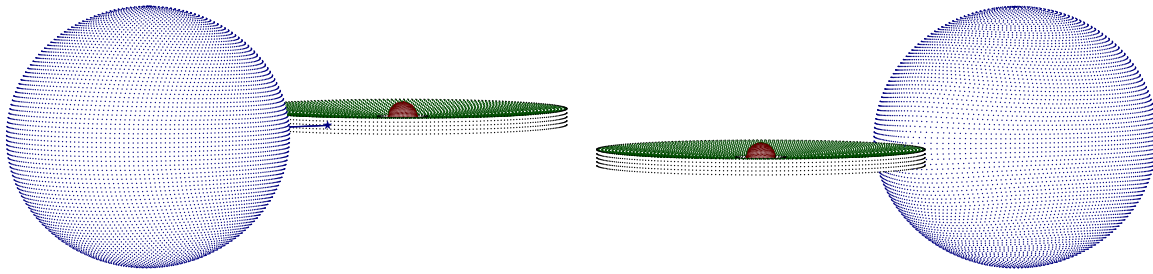


Figure 6. Visualization of the grids used to model ZTF J2130+4420 seen at orbital phases 0.4 (left) and 0.9 (right). The actual grids used had a higher resolution than those displayed here.

number of parallel chains to explore the solution space. We used 256 chains and let them run until the chains stabilized to a solution, which took approximately 2000 generations.

Figure 6 shows visualizations of the model grids, showing the approximate geometry and sizes of the various components adopted. The gas stream and bright spot, although illustrated, were not used during model computations. Figure 7 shows the fit for each HiPERCAM band, and Figure 8 shows the corner plot for the best solution from the MCMC sampler.

5. System Parameters

The strong light-curve variability caused by ellipsoidal modulation and the eclipsing accretion disk, in combination with the RV amplitude and spectral fits, allow us to derive system parameters. Solutions were calculated from a simultaneous fit to the five HiPERCAM light curves (Table 4).

We find that the system consists of a low-mass sdOB with a typical WD companion. The sdOB is Roche lobe–filling and has a volumetric-corrected radius of $R_{\text{sdOB}} = 0.124 \pm 0.005 R_{\odot}$. A mass ratio $q = M_{\text{sdOB}}/M_{\text{WD}} = 0.617 \pm 0.015$, a mass for the sdOB $M_{\text{sdOB}} = 0.337 \pm 0.015 M_{\odot}$, and a WD companion mass $M_{\text{WD}} = 0.545 \pm 0.020 M_{\odot}$ were derived. The mass of the sdOB is significantly lower than for a canonical sdOB with $\approx 0.48 M_{\odot}$. The radius of the sdOB star is found to be typical for an sdOB star, and the inclination is found to be $i = 86.4 \pm 1.0^{\circ}$ (Table 4). From the system parameters, we find that the sdOB would have a projected rotational velocity $v_{\text{rot}} \sin i = 227 \pm 10 \text{ km s}^{-1}$ if synchronized to the orbit. The measured $v_{\text{rot}} \sin i = 238 \pm 15 \text{ km s}^{-1}$ is consistent with a synchronized orbit.

We calculate the absolute magnitude (M_g) of ZTF J2130+4420 using the visual PanSTARRS g -band magnitude ($m_g = 15.33 \pm 0.01 \text{ mag}$; Chambers et al. 2016) and the parallax from the *Gaia* Data Release 2 (DR2; $\varpi = 0.8329 \pm 0.0305 \text{ mas}$; Gaia Collaboration et al. 2016, 2018). Because ZTF J2130+4420 is located near the Galactic plane, significant reddening can occur. Green et al. (2019) presented updated 3D extinction maps based on *Gaia* parallaxes and stellar photometry from PanSTARRS 1 and the Two Micron All Sky Survey²² and found toward the direction of ZTF J2130+4420 an extinction of $E(g-r) = 0.18 \pm 0.02$ at a distance of $1.2 \pm 0.06 \text{ kpc}$; this results in a total extinction in the g band of $A_g = 0.63 \text{ mag}$. With the corrected magnitude, we find an absolute magnitude of $M_g = 4.3 \pm 0.2 \text{ mag}$, consistent with a hot subdwarf star (Geier et al. 2019).

6. Discussion

6.1. Comparison with *Gaia* Parallax

To test whether our derived system parameters are consistent with the parallax provided by the *Gaia* DR2 ($\varpi = 0.8329 \pm 0.0305 \text{ mas}$), we compared the measured parameter from the light-curve fit to the predictions using the *Gaia* parallax. The approach follows a similar strategy to that described by Ratzloff et al. (2019). Using the absolute magnitude $M_g = 4.3 \pm 0.2 \text{ mag}$, we calculate the luminosity:

$$L_{\text{sdOB}} = L_{\odot} 10^{-0.4(M_g + \text{BC}_g)}. \quad (2)$$

With $L_{\odot} = 3.0128 \times 10^{33} \text{ erg s}^{-1}$ and a bolometric correction $\text{BC}_g = -3.6 \text{ mag}$ derived for our stellar parameters from the MESA Isochrones & Stellar Tracks (MIST; Paxton et al. 2011, 2013, 2015, 2018; Choi et al. 2016; Dotter 2016), we find $L_{\text{sdOB}} = 41 \pm 9 L_{\odot}$. Using the Stefan–Boltzmann law applied to a blackbody ($L = 4\sigma\pi R_{\text{sdOB}}^2 T_{\text{eff}}^4$), we solve for the radius of the sdOB star, and, combined with $R_{\text{sdOB}}^2 = GM_{\text{sdOB}}/g$, we derive the sdOB mass,

$$M_{\text{sdOB}} = \frac{L_{\text{sdOB}} 10^{\log g}}{4\pi G T_{\text{eff}}^4}, \quad (3)$$

giving $M_{\text{sdOB}} = 0.30 \pm 0.08 M_{\odot}$ and a radius $R_{\text{sdOB}} = 0.12 \pm 0.02 R_{\odot}$; both are in agreement with the results from the light-curve and spectroscopic fits and confirm that this sdOB star is lower in mass than the canonical hot subdwarf stars.

6.2. Evolutionary History

In order to match the high T_{eff} observed with a hot subdwarf that still retains some surface hydrogen, we construct binary evolution models of hot subdwarfs that come into contact with a WD companion only after they have completed core helium burning and evolved toward hotter temperatures. We use MESA version 12115 to construct these models (Paxton et al. 2011, 2013, 2015, 2018, 2019). We start by constructing low-mass He-burning hot subdwarf models from progenitors with masses in the range $2.5\text{--}2.8 M_{\odot}$, which have main-sequence lifetimes of $400\text{--}500 \text{ Myr}$. After evolving onto the red giant branch (RGB), these stars achieve core temperatures high enough for nondegenerate helium ignition and hence can form He-burning cores with masses lower than the $0.48 M_{\odot}$ required for a degenerate He core flash. Figure 9 shows the internal composition profile for a $2.8 M_{\odot}$ RGB model as it begins central He burning. Main-sequence stars in this mass range develop convective cores that initially encompass $\approx 0.5 M_{\odot}$ but then recede to encompass less than $0.2 M_{\odot}$ by

²² <http://argonaut.skymaps.info/>

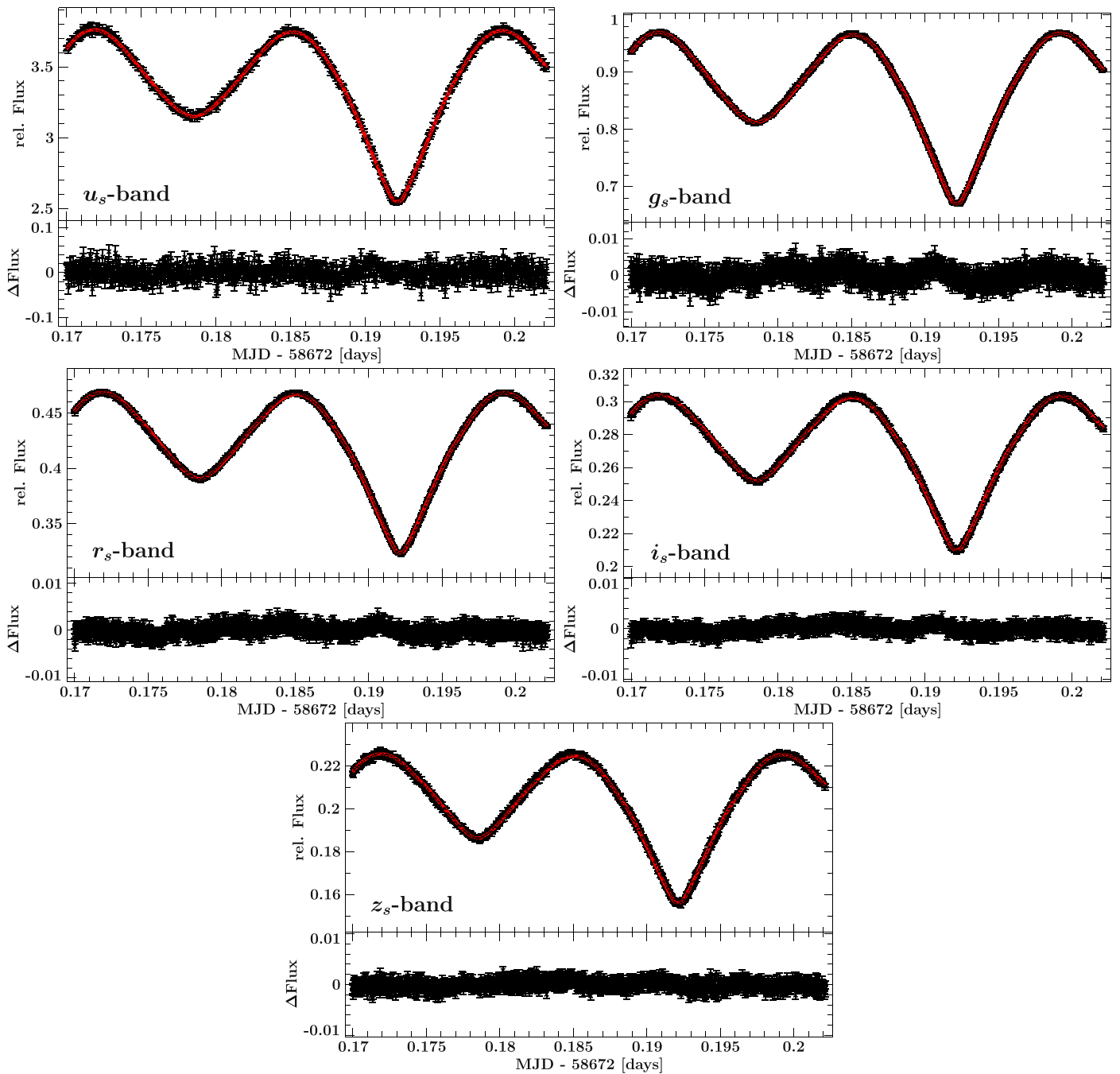


Figure 7. HiPERCAM light curves (black) shown together with the LCURVE fits (red) for all five simultaneously observed optical Super-SDSS bandpasses.

the end of core hydrogen burning. After the He core forms and begins to grow as the star ascends the RGB, the region outside the He core reflects a composition that has been partially processed by nuclear burning, with H still present but less abundant than its primordial value. Because the convective core burning on the main sequence is dominated by the CNO cycle, we also expect that the interior region that eventually forms the hot subdwarf will be depleted of carbon and rich in nitrogen.

Once these models begin core He burning, we remove most of the mass of the outer envelope, leaving only $\approx 0.01 M_{\odot}$ of H/He envelope material outside the He-dominated core. The star then evolves to become an He-burning hot subdwarf. The left panel of Figure 10 shows evolutionary tracks for a selection

of these hot subdwarf models varying both the He core mass and envelope mass. Our MESA models for this stage employ the predictive mixing scheme for convection to allow proper growth of the convective core and yield correct He-burning lifetimes (Paxton et al. 2018). These models are relatively low-mass and low-luminosity for hot subdwarfs, and core He burning lasts approximately 500 Myr. This stage corresponds to the portion of the tracks in the lower-temperature ($T_{\text{eff}} \leq 30,000$ K) regime in Figure 10. Once burning exhausts He in the core, the model evolves toward hotter temperatures over a timescale of order 10 Myr. The core contracts, and residual H in the envelope begins to burn in a shell, pushing the surface to a larger radius and forming the hotter peak in the tracks shown in Figure 10. The left panel of Figure 10 shows

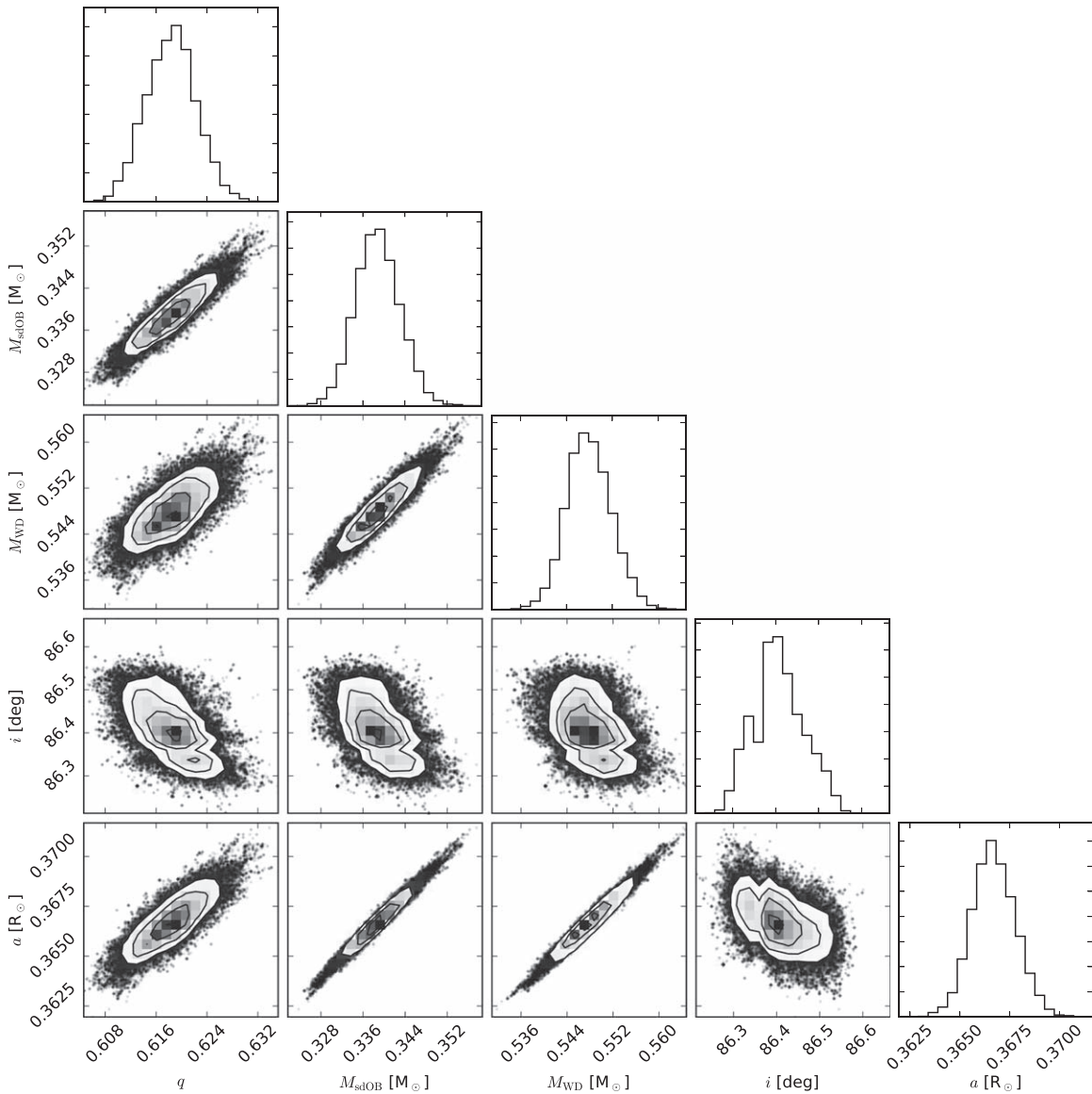


Figure 8. Corner plots of the physical parameters inferred as a result of the analysis combining the light-curve modeling with RV and spectral line fitting results.

that we prefer a mass slightly higher than $0.33 M_{\odot}$ to achieve a high enough temperature to match our observations and a relatively thick H/He envelope to achieve a radius consistent with the measured $\log(g)$.

For the most massive of our four hot subdwarf models, we perform a MESA binary evolution calculation with a $0.55 M_{\odot}$ WD companion initialized with an orbital period of 148 minutes at the beginning of core He burning. The right panel of Figure 10 shows the evolutionary track compared to the single-star model and the radius constraint due to its binary Roche lobe (gray shaded region). For the binary evolution, Roche lobe radii are computed using the fit of Eggleton (1983), and mass transfer rates follow the prescription of Ritter (1988) when the donor star overflows its Roche lobe. In our MESA models, the binary separation evolves according to gravitational-wave radiation and angular momentum conservation of material transferred from the donor to its companion (Paxton et al. 2015). We treat the accreting WD as a point mass that accretes all material lost by the Roche lobe–overflowing donor star.

In our binary evolution model, the orbit decays due to gravitational-wave losses over the core He-burning lifetime, but not enough to bring the star into contact with its WD companion at this stage. Instead, the core contracts as He is exhausted in the center, and this causes the residual H shell to begin burning. The expansion driven by this shell burning pushes the radius outward to overflow its Roche lobe at an orbital period of 40.5 minutes. The evolution of the envelope drives mass transfer at a rate of $10^{-9} M_{\odot} \text{yr}^{-1}$ lasting approximately 1 Myr as the subdwarf continues to evolve toward hotter temperatures. Accretion onto the WD companion at this rate will cause unstable hydrogen ignition after $\approx 10^{-4} M_{\odot}$ accumulates, leading to a classical nova eruption (Nomoto 1982; Nomoto et al. 2007; Wolf et al. 2013). This accretion rate therefore predicts a recurrence time of order 10^5 yr for a total of approximately 10 novae. The novae will cause some mass to be lost from the system, and this effect is not captured in our modeling, where we treat the accretor as a point mass that retains all accreted mass. However, the total amount of mass lost by the donor through this phase is only

Table 4

Overview of the Measured and Derived Parameters for ZTF J2130+4420

R.A. ^a	R.A. (hr)	21:30:56.71
decl. ^a	decl. (deg)	44:20:46.450
Magnitude ^b	g (mag)	15.33 ± 0.01
Parallax ^a	ϖ (mas)	0.8329 ± 0.0305
Distance	d (kpc)	1.20 ± 0.06
Absolute magnitude (reddening corrected)	M_g (mag)	4.3 ± 0.2
Proper motion (R.A.)	$\mu_{\alpha} \cos(\delta)$ (mas yr ⁻¹)	0.009 ± 0.047
Proper motion (decl.)	μ_{δ} (mas yr ⁻¹)	-1.682 ± 0.048
Atmospheric Parameters of the sdOB		
Effective temperature	T_{eff} (K)	$42,400 \pm 300$
Surface gravity	$\log(g)$	5.77 ± 0.05
Helium abundance	$\log y$	-0.52 ± 0.03
Projected rotational velocity	$v_{\text{rot}} \sin i$ (km s ⁻¹)	238 ± 15
Orbital Parameters		
Ephemeris zero-point	T_0 (MJD)	58,672.18085(78)
Orbital period	P_{orb} (minutes)	39.3401(1)
RV semi-amplitude (sdOB)	K (km s ⁻¹)	418.5 ± 2.5
System velocity	γ (km s ⁻¹)	-33.9 ± 1.9
Binary mass function	f_m (M_{\odot})	0.2075 ± 0.0037
Derived Parameters		
Mass ratio	$q = \frac{M_{\text{sdOB}}}{M_{\text{WD}}}$	0.617 ± 0.015
sdOB mass	M_{sdOB} (M_{\odot})	0.337 ± 0.015
sdOB radius	R_{sdOB} (R_{\odot})	0.125 ± 0.005
WD mass	M_{WD} (M_{\odot})	0.545 ± 0.020
Orbital inclination	i (deg)	86.4 ± 1.0
Separation	a (R_{\odot})	0.367 ± 0.004

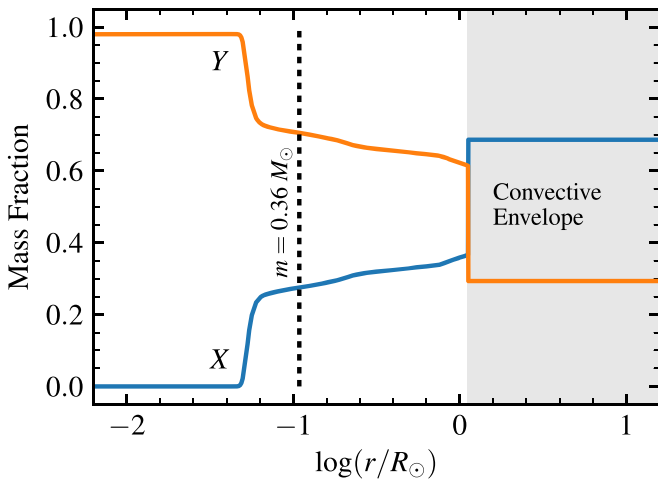
Notes.^a From *Gaia* DR2 (Gaia Collaboration et al. 2018).^b From PanSTARRS DR1 (Chambers et al. 2016).

Figure 9. Hydrogen (X) and helium (Y) composition profile for a $2.8 M_{\odot}$ RGB star just before core helium burning begins and outer material is removed to make a hot subdwarf. The black dashed line shows the location of mass coordinate $m = 0.36 M_{\odot}$ corresponding to the surface of the hot subdwarf after the envelope is removed. Nuclear burning has partially processed the material at this location due to a former convective core that receded over the duration of the main sequence.

$10^{-3} M_{\odot}$, so the mass transfer efficiency will not have a significant impact on the orbital evolution.

Figure 11 shows the evolution of the donor through this mass transfer phase, which ends just $\approx 10^5$ yr before the system reaches the currently observed orbital period and temperature.

After 1 Myr of mass transfer, hydrogen burning ceases and the subdwarf contracts to become a WD. While this particular binary evolution model points to a recent cessation of mass transfer in this system, we caution that this may not be a generic feature for the family of hot subdwarf models presented here. The precise configuration of mass transfer in relation to the evolution of T_{eff} and $\log(g)$ is sensitive to both core and envelope mass, and we leave a full exploration of this space of models to other work. We note that in our models, there is no He shell-burning phase, so the resulting WD retains a substantial ($\approx 0.15 M_{\odot}$) He layer. While this final He layer mass is subject to theoretical uncertainties in the physics of convective mixing and burning near core He depletion, which affects subsequent He shell structure, models generically predict that $\approx 0.1 M_{\odot}$ of He will remain after He burning has ceased for subdwarf stars of this mass. This significant mass of He may lead to a thermonuclear supernova in ≈ 17 Myr when gravitational waves bring the system into contact again as a double WD binary (Perets et al. 2019; Zenati et al. 2019). If the system does not explode as a thermonuclear supernova, the most likely outcome is a double WD merger and subsequent evolution into an R CrB star with a mass of $0.8\text{--}0.9 M_{\odot}$, which is the most common mass range for R CrB stars (Saio 2008; Clayton 2012). To prevent the merger and form a stable AM CVn-type system, the system requires a very strong dissipative coupling of the accretor to the orbit and synchronization timescale of $\tau_s \lesssim 0.1$ yr (Marsh et al. 2004).

6.3. Kinematics of ZTF J2130+4420

If the sdOB star has evolved from a $2.5\text{--}2.8 M_{\odot}$ star, the system has to be part of a young population. To put constraints on the population origin of ZTF J2130+4420, we calculated its kinematics. The proper motions of the system are taken from the *Gaia* DR2 catalog (Gaia Collaboration et al. 2018; $\mu_{\alpha} \cos(\delta) = 0.009 \pm 0.047$ mas yr⁻¹, $\mu_{\delta} = -1.682 \pm 0.048$ mas yr⁻¹). The distance was taken as 1.20 ± 0.06 kpc, as derived from the *Gaia* parallax (see Section 5), and the systemic velocity was taken from the RV curve ($\gamma = -33.9 \pm 1.9$ km s⁻¹; see Section 3).

We employed the approach described in Odenkirchen & Brosche (1992) and Pauli et al. (2006). We use the Galactic potential of Allen & Santillan (1991) as revised by Irrgang et al. (2013). The orbit was integrated from the present to 3 Gyr into the past. The kinematics of ZTF J2130+4420 are visualized in Figure 12, where the two panels show the orbit projected on to the x - y and $R = \sqrt{x^2 + y^2}$ - z planes, x , y , z being Galactic coordinates. The object moves within a height of 100 pc of the Galactic equator. From the Galactic orbit, we conclude that ZTF J2130+4420 is a member of the Galactic thin disk population.

6.4. Helium WD Interpretation for the Donor Star

Kupfer et al. (2017a) reported the discovery of a similar sdOB+WD system with an orbital period of 44 minutes and $T_{\text{eff}} = 39,400$ K but no obvious signs of an accretion disk. Their interpretation of that discovery was that the sdOB star in that system is a young He core WD that is just beginning to cool, and that the binary had exited the common envelope phase within the last Myr. We cannot rule out a similar interpretation for the system presented here, but we prefer the binary evolution models that we present in this work as a more

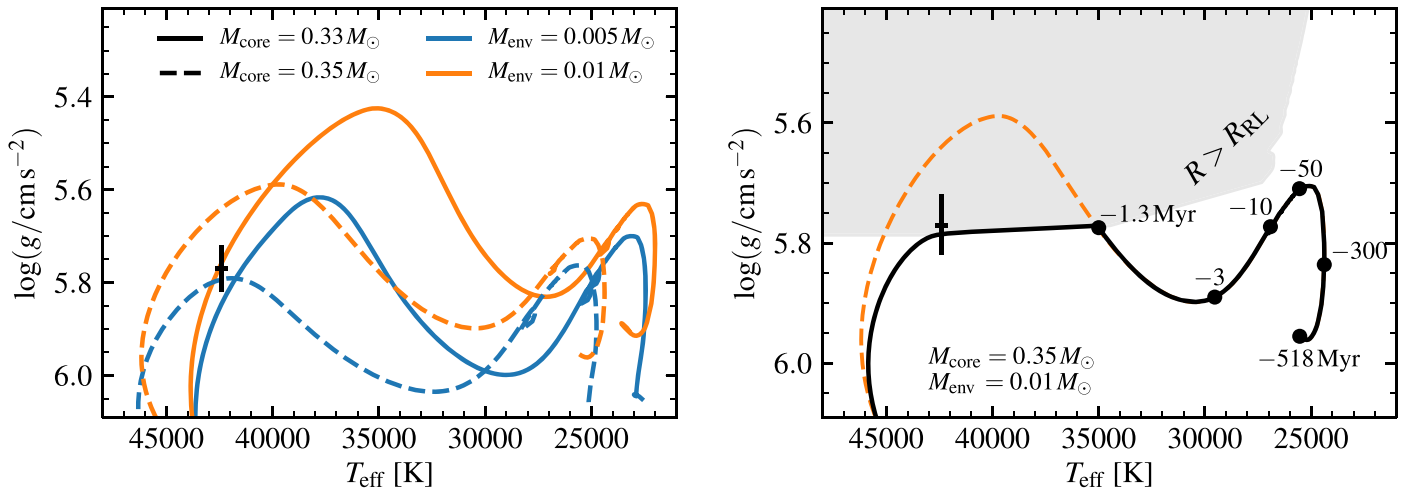


Figure 10. Left: evolutionary tracks for hot subdwarf models with two values of He mass and envelope mass. The black cross corresponds to the observational constraints given in Table 4. Tracks start on the lower right of the plot and evolve leftward toward hotter temperatures when core He is exhausted. Right: binary evolution track for the most massive of our hot subdwarf models. The gray shaded region shows the maximum radius R that the subdwarf can reach before overflowing its Roche lobe radius R_{RL} , which shrinks over time due to gravitational-wave radiation. The black points label ages (in Myr) along the track relative to the present time.

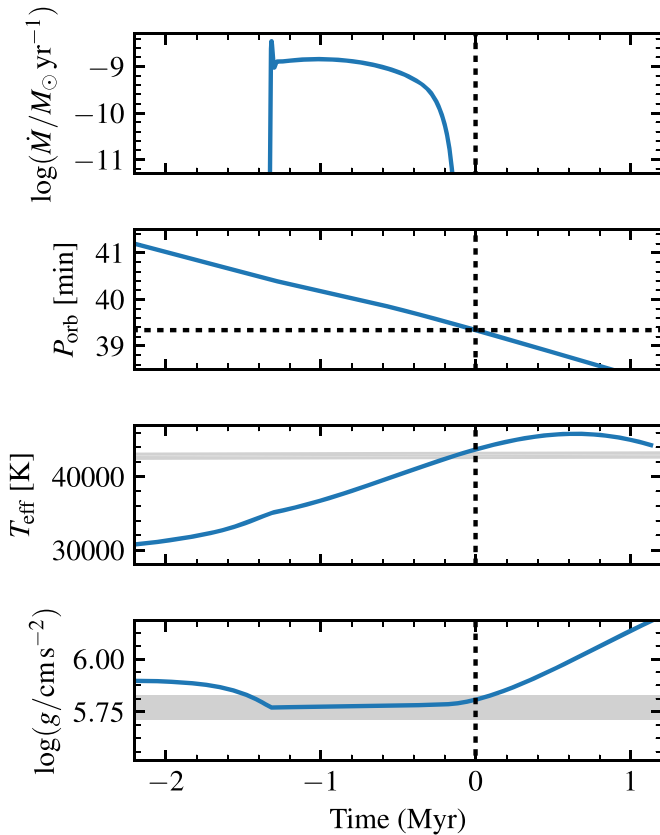


Figure 11. Time evolution of the MESA binary model through the mass transfer phase leading up to the currently observed state defined by $P_{\text{orb}} = 39.34$ minutes at time 0. Gray shaded regions in the lower two panels show the measured values of T_{eff} and $\log(g)$ given in Table 4.

natural explanation for the presence of an accretion disk as a result of recent Roche lobe overflow and mass transfer. We note that an accretion disk around the companion WD cannot be ruled out for the Kupfer et al. (2017a) system, as the sdOB would outshine an accretion disk and its inclination is too low to show eclipses. Therefore, that system may also be consistent

with a binary scenario from the family of models we present in this work.

6.5. WD Accretor Mass

We find a mass for the WD companion $M_{\text{WD}} = 0.545 \pm 0.020 M_{\odot}$, which is slightly below the typical mass of $0.6 M_{\odot}$. In the standard picture, the WD companion was formed first; therefore, the main-sequence mass of the WD companion had to be larger than the main-sequence mass of the sdOB star, which we found earlier to be $2.5\text{--}2.8 M_{\odot}$. Cummings et al. (2018) presented the initial–final mass relation (IFMR) based on 73 WDs for isolated WDs. Using Equation (4) from that analysis, we find that a main-sequence star with $M = 2.8 M_{\odot}$ will form a WD with $M_{\text{WD}} = 0.71 \pm 0.09 M_{\odot}$, which is inconsistent with our result.

Kalirai et al. (2014) showed that the core mass—and hence the WD mass—grows by $\approx 10\%$ for stars with initial masses of $\approx 3 M_{\odot}$ on the asymptotic giant branch (AGB). It is likely that the progenitor of the WD companion experienced a phase of mass transfer on the AGB, where the star lost its envelope before the core had grown to its final mass predicted by the IFMR for isolated WDs and instead formed a WD with a mass $\approx 10\%$ below the IFMR prediction and hence ended up with a mass consistent with our observed value.

6.6. An Unusual Accretion Disk

The accretion disk in ZTF J2130+4420 is unusual in that it is heavily irradiated by the mass donor. This has one important consequence: even if the accretion rate is significantly lower than we estimate, such that one would normally expect to see dwarf nova outbursts, it could be that the irradiation from the donor suppresses the outbursts by keeping the disk in a permanent high state, as has been hypothesized to explain the long outbursts of some X-ray transients (King & Ritter 1998).

Our high S/N WHT spectra ($S/N \approx 100$) show no evidence of any disk lines. Therefore, we can limit the contribution of the accretion disk to the overall luminosity to $\leq 3\%$. Our models predict an accretion rate of $10^{-9} M_{\odot} \text{ yr}^{-1}$ or even lower if the system is close to the cessation of its accretion phase.

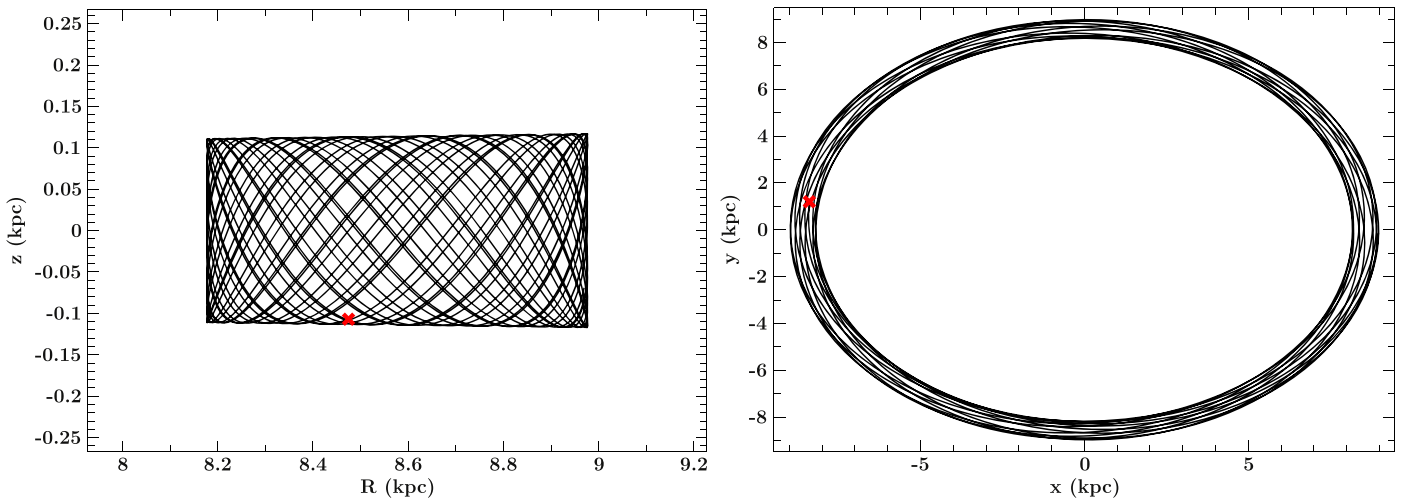


Figure 12. Left: orbit of ZTF J2130+4420 projected onto the x - y plane. Right: orbit projected in the R , z plane, with $R = \sqrt{x^2 + y^2}$. Here x , y , and z are the Galactic coordinates of the source. The red dot shows the current location of ZTF J2130+4420.

From that, we can limit the accretion luminosity to be $< 1 L_{\odot}$, which is significantly smaller than the luminosity of the sdOB star ($L_{\text{sdOB}} = 41 \pm 9 L_{\odot}$; see Section 6.1) and in agreement with the absence of any signs of the disk in the optical spectra.

Rivera Sandoval et al. (2019) reported the nondetection of X-rays in a 1 ks observation with the *Neil Gehrels Swift Observatory*. The X-rays from disk-accreting WDs are generally emitted from the boundary layer. However, with an increasing accretion rate, the boundary layer becomes optically thick to its own radiation, and emission shifts from the X-ray region to the extreme ultraviolet (Pringle & Savonije 1979; Patterson & Raymond 1985). Such accretion disks are less luminous in the X-ray, despite their higher accretion rates. This was observed by Wheatley et al. (2003), who conducted a multiwavelength campaign during a dwarf nova outburst of SS Cyg. They showed that during the outburst, as the accretion increases, the X-ray luminosity drops and the extreme UV emission increases. This illustrates the rather complex relation between accretion rate and X-ray flux and perhaps can explain the nondetection of X-rays in ZTF J2130+4420. However, we cannot exclude that our models overestimate the accretion rate, in particular if the sdOB donor is close to the end of mass transfer. We encourage deeper X-ray observations in the future.

6.7. Gravitational Waves

Due to its short period, ZTF J2130+4420 is expected to be a strong source of gravitational waves and might be detectable with the *Laser Interferometer Space Antenna (LISA)* as an individual source (Amaro-Seoane et al. 2017). The gravitational-wave strain amplitude h scales with the masses of both binary components, the binary inclination, the orbital period, and the distance of the system.

Based on Kupfer et al. (2018, and references therein), we can calculate the dimensionless gravitational-wave amplitude (\mathcal{A}),

$$\mathcal{A} = \frac{2(G\mathcal{M})^{5/3}}{c^4 d} (\pi f)^{2/3}, \quad (4)$$

where \mathcal{M} is the chirp mass, $\mathcal{M} \equiv (M_{\text{sdOB}} M_{\text{WD}})^{3/5} / (M_{\text{sdOB}} + M_{\text{WD}})^{1/5}$, d is the distance, and f is the gravitational-wave frequency with $f = 2/P_{\text{orb}}$. We find $\mathcal{A} = (8.40 \pm 0.65) \times 10^{-23}$.

We can then calculate the characteristic strain (h_c),

$$h_c = \sqrt{N_{\text{cycle}}} \mathcal{A}, \quad (5)$$

where $N_{\text{cycle}} = f T_{\text{obs}}$. Assuming the nominal mission lifetime of 4 yr, we find $h_c = (1.96 \pm 0.14) \times 10^{-20}$. For the extended mission lifetime of 10 yr, we find $h_c = (3.10 \pm 0.22) \times 10^{-20}$. Although its high inclination disfavors the S/N for *LISA*, the presence of an eclipse allows for the determination of the binary parameter to a high accuracy and hence a precise prediction of the gravitational-wave strain. Using the approach described in Burdge et al. (2019), we find an S/N for *LISA* of ≈ 3 assuming a 4 yr lifetime and ≈ 5 assuming a 10 yr lifetime.

Assuming the evolution of the system is governed by gravitational-wave radiation, we can predict the orbital decay of the system \dot{P} :

$$\dot{P} = \frac{192}{5} \pi^{8/3} \left(\frac{G^{5/3} M_{\text{sdOB}} M_{\text{WD}} P_{\text{orb}}^{-5/3}}{c^5 (M_{\text{sdOB}} + M_{\text{WD}})^{1/3} 2^{-5/3}} \right). \quad (6)$$

Using this equation, we find $\dot{P} = (-1.68 \pm 0.42) \times 10^{-12} \text{ s s}^{-1}$. Given the sharp eclipses of the accretion disk, this should be detectable after a few years of monitoring.

6.8. Selection Effect

The residual hydrogen shell-burning lifetime of the hot subdwarf with $M_{\text{sdOB}} = 0.35 M_{\odot}$ in ZTF J2130+4420 is a factor of ≈ 50 –100 shorter than its helium core-burning lifetime; hence, finding ZTF J2130+4420 at the end of hydrogen shell burning means that there should be at least a few tens of detached low-mass hot subdwarfs with WD companions at $P_{\text{orb}} \lesssim 2.5$ hr. So far, only four helium core-burning hot subdwarfs are known to have a WD companion and $P_{\text{orb}} \lesssim 2.5$ hr: CD $-30^{\circ}11223$ ($P_{\text{orb}} = 70.5$ min; Vennes et al. 2012; Geier et al. 2013), PTF1 J0823+0819 ($P_{\text{orb}} = 87$ minutes; Kupfer et al. 2017b), KPD 0422+5421 ($P_{\text{orb}} = 129$ minutes; Koen et al. 1998; Orosz & Wade 1999), and KPD 1930+2752 ($P_{\text{orb}} = 136$ minutes; Maxted et al. 2000; Geier et al. 2007). Only CD $-30^{\circ}11223$ will start mass transfer to the WD during He core burning, whereas PTF1 J0823+0819 might start accreting toward the end of He shell burning.

Initially, ZTF J2130+4420 was discovered in a search for periodic objects in the Geier et al. (2019) hot subdwarf catalog of $\approx 40,000$ hot subdwarf candidates. Photometric surveys like the ZTF are only sensitive to hot subdwarf binaries with compact companions if the sdB star shows at least a few percent photometric amplitudes from ellipsoidal deformation; hence, the sdB has to be close to Roche lobe filling. As shown in Figure 10, an object like ZTF J2130+4420 is far from Roche lobe filling during He core burning and would not show any photometric variability.

A different way to detect compact sdB binaries is from large RV shifts on short timescales. The MUCHFUSS survey used this strategy to find compact hot subdwarf binaries (Geier et al. 2011) in Sloan Digital Sky Survey (SDSS) multi-epoch spectra, and indeed, CD $-30^\circ 11223$ was first identified from large RV shifts on short timescales. When the binary had $P_{\text{orb}} \approx 2$ hr, ZTF J2130+4420 would show a velocity semi-amplitude of $K \approx 250\text{--}300$ km s $^{-1}$ during He core burning. This would be easily detectable in low-resolution multi-epoch spectra such as those taken in SDSS with the BOSS spectrograph. However, the hot subdwarf in ZTF J2130+4420 has evolved from a $2.5\text{--}2.8 M_\odot$ main-sequence star and therefore has to be a young system that is consistent with its kinematics. The SDSS almost exclusively observed hot subdwarfs at high Galactic latitudes and therefore did not cover the young population of hot subdwarf binaries. Future multi-epoch spectroscopic surveys that cover lower Galactic latitudes will be able to detect a substantial number of progenitor systems of ZTF J2130+4420.

7. Conclusion and Summary

As part of a search for periodic objects in the Geier et al. (2019) hot subdwarf candidate catalog, ZTF J2130+4420 was discovered as a short-period variable with a remarkable light-curve shape. Follow-up observations show that ZTF J2130+4420 is an ultracompact sdOB binary with a compact companion with $P_{\text{orb}} = 39.3401(1)$ minutes, making it the most compact hot subdwarf binary known today.

High-S/N photometry obtained with HiPERCAM allows us to put tight constraints on the system parameters. We find that we can only fit the HiPERCAM light curve when including an irradiated accretion disk, making ZTF J2130+4420 the first known hot subdwarf binary where the sdOB filled its Roche lobe and started mass transfer to its WD companion. Combining the HiPERCAM light curves with spectroscopy, we find a mass ratio $q = M_{\text{sdOB}}/M_{\text{WD}} = 0.617 \pm 0.015$, a mass for the sdOB $M_{\text{sdOB}} = 0.337 \pm 0.015 M_\odot$, and a WD companion mass $M_{\text{WD}} = 0.545 \pm 0.020 M_\odot$. The derived sdOB mass is consistent with the estimate from the *Gaia* parallax and lower than the canonical mass for hot subdwarfs of $\approx 0.47 M_\odot$. Therefore, the sdOB has not evolved from the standard hot subdwarf channel where the envelope of the hot subdwarf progenitor gets stripped at the tip of the RGB. Instead, it has likely evolved from a $2.5\text{--}2.8 M_\odot$ progenitor that was stripped when crossing the Hertzsprung gap. Therefore, the system has to be young, which is consistent with the observed kinematics.

To put constraints on the evolutionary history of the system, we compared the derived P_{orb} , T_{eff} , $\log(g)$, and mass to evolutionary tracks for He stars computed with MESA. We find that the binary left the common envelope when the hot subdwarf was formed at $P_{\text{orb}} \approx 150$ minutes and reached contact at $P_{\text{orb}} \approx 40$ minutes during residual hydrogen shell

burning when the envelope started to expand again. We currently observe the object toward the end of hydrogen shell burning. Once hydrogen shell burning is finished, the sdOB will shrink within its Roche lobe, and the binary will reach contact again after ≈ 17 Myr as a double WD. The system will either explode as a thermonuclear supernova (Perets et al. 2019; Zenati et al. 2019) or form an R CrB star.

Although the He core-burning lifetime is a factor of ≈ 100 larger compared to the residual hydrogen shell-burning lifetime, current surveys are not sensitive enough to detect such systems when they are part of the young stellar population and far away from Roche lobe filling. Ongoing and upcoming multi-epoch spectroscopic surveys that cover low Galactic latitudes, like LAMOST (Deng et al. 2012), SDSS-V (Kollmeier et al. 2017), WEAVE (Dalton et al. 2012), or 4MOST (de Jong et al. 2019), will be sensitive to exploring the young population of detached sdB binaries with compact companions and periods \lesssim a few hours.

Based on observations obtained with the Samuel Oschin Telescope 48 inch at the Palomar Observatory as part of the Zwicky Transient Facility project. The ZTF is supported by the National Science Foundation under grant No. AST-1440341 and a collaboration including Caltech, IPAC, the Weizmann Institute for Science, the Oskar Klein Center at Stockholm University, the University of Maryland, the University of Washington, Deutsches Elektronen-Synchrotron and Humboldt University, Los Alamos National Laboratories, the TANGO Consortium of Taiwan, the University of Wisconsin at Milwaukee, and Lawrence Berkeley National Laboratories. Operations are conducted by COO, IPAC, and UW.

Some of the data presented herein were obtained at the W.M. Keck Observatory, which is operated as a scientific partnership among the California Institute of Technology, the University of California, and the National Aeronautics and Space Administration. The Observatory was made possible by the generous financial support of the W.M. Keck Foundation. The authors wish to recognize and acknowledge the very significant cultural role and reverence that the summit of Maunakea has always had within the indigenous Hawaiian community. We are most fortunate to have the opportunity to conduct observations from this mountain.

Some results presented in this paper are based on observations made with the WHT, operated on the island of La Palma by the Isaac Newton Group in the Spanish Observatorio del Roque de los Muchachos of the Instituto de Astrofísica de Canarias.

Based on observations made with the Gran Telescopio Canarias (GTC), installed at the Spanish Observatorio del Roque de los Muchachos of the Instituto de Astrofísica de Canarias on the island of La Palma.

The KPED team thanks the National Science Foundation and the National Optical Astronomical Observatory for making the Kitt Peak 2.1 m telescope available. The KPED team thanks the National Science Foundation, the National Optical Astronomical Observatory, and the Murty family for support in the building and operation of KPED.

This research was supported in part by the National Science Foundation through grant ACI-1663688 and at the KITP by grant PHY-1748958. This research benefited from interactions that were funded by the Gordon and Betty Moore Foundation through grant GBMF5076.

We acknowledge the use of the Center for Scientific Computing, supported by the California NanoSystems Institute and the Materials Research Science and Engineering Center (MRSEC) at UC Santa Barbara, through NSF DMR 1720256 and NSF CNS 1725797.

HiPERCAM and VSD are funded by the European Research Council under the European Union's Seventh Framework Programme (FP/2007-2013) under ERC-2013-ADG grant agreement No. 340040 (HiPERCAM).

We thank Brad Barlow, Josiah Schwab, and Stephan Geier for helpful conversations. M.C. is supported by the David and Ellen Lee Postdoctoral Fellowship at the California Institute of Technology. T.R.M. was supported by a grant from the United Kingdom's Science and Technology Facilities Council. P.S. acknowledges support from NSF grant AST-1514737.

This work has made use of data from the European Space Agency (ESA) mission *Gaia* (<https://www.cosmos.esa.int/gaia>), processed by the *Gaia* Data Processing and Analysis Consortium (DPAC; <https://www.cosmos.esa.int/web/gaia/dpac/consortium>). Funding for the DPAC has been provided by national institutions, in particular the institutions participating in the *Gaia* Multilateral Agreement.

This work benefited from a workshop held at DARK in 2019 July that was funded by the Danish National Research Foundation (DNRF132). We thank Josiah Schwab for his efforts in organizing this.

Facilities: PO:1.2 m (ZTF), Hale (DBSP), Keck:I (LRIS), ING:Herschel (ISIS), GTC (HiPERCAM).

Software: Lpipe (Perley 2019), PyRAF (Bellm & Sesar 2016), Gatspy (VanderPlas & Ivezić 2015; Vanderplas 2015), FITSB2 (Napiwotzki et al. 2004), LCURVE (Copperwheat et al. 2010), emcee (Foreman-Mackey et al. 2013), MESA (Paxton et al. 2011, 2013, 2015, 2018, 2019), Matplotlib (Hunter 2007), Astropy (Astropy Collaboration et al. 2013, 2018), Numpy (Oliphant 2015).

ORCID iDs

Thomas Kupfer  <https://orcid.org/0000-0002-6540-1484>
 Evan B. Bauer  <https://orcid.org/0000-0002-4791-6724>
 Thomas R. Marsh  <https://orcid.org/0000-0002-2498-7589>
 Jan van Roestel  <https://orcid.org/0000-0002-2626-2872>
 Eric C. Bellm  <https://orcid.org/0000-0001-8018-5348>
 Kevin B. Burdge  <https://orcid.org/0000-0002-7226-836X>
 Michael W. Coughlin  <https://orcid.org/0000-0002-8262-2924>
 Jim Fuller  <https://orcid.org/0000-0002-4544-0750>
 JJ Hermes  <https://orcid.org/0000-0001-5941-2286>
 Shrinivas R. Kulkarni  <https://orcid.org/0000-0001-5390-8563>
 Thomas A. Prince  <https://orcid.org/0000-0002-8850-3627>
 Paula Szkody  <https://orcid.org/0000-0003-4373-7777>
 Vik S. Dhillon  <https://orcid.org/0000-0003-4236-9642>
 Gabriel Murawski  <https://orcid.org/0000-0001-7809-1457>
 Dmitry A. Dhev  <https://orcid.org/0000-0001-5060-8733>
 Matthew J. Graham  <https://orcid.org/0000-0002-3168-0139>
 David L. Kaplan  <https://orcid.org/0000-0001-6295-2881>
 Russ R. Laher  <https://orcid.org/0000-0003-2451-5482>
 S. P. Littlefair  <https://orcid.org/0000-0001-7221-855X>
 Frank J. Masci  <https://orcid.org/0000-0002-8532-9395>
 Reed Riddle  <https://orcid.org/0000-0002-0387-370X>
 Ben Rusholme  <https://orcid.org/0000-0001-7648-4142>
 David L. Shupe  <https://orcid.org/0000-0003-4401-0430>

Maayane T. Soumagnac  <https://orcid.org/0000-0001-6753-1488>

References

- Allen, C., & Santillan, A. 1991, *RMxAA*, **22**, 255
 Amaro-Seoane, P., Audley, H., Babak, S., et al. 2017, arXiv:1702.00786
 Astropy Collaboration, Price-Whelan, A. M., Sipőcz, B. M., et al. 2018, *AJ*, **156**, 123
 Astropy Collaboration, Robitaille, T. P., Tollerud, E. J., et al. 2013, *A&A*, **558**, A33
 Bauer, E. B., Schwab, J., & Bildsten, L. 2017, *ApJ*, **845**, 97
 Bellm, E. C., Kulkarni, S. R., Barlow, T., et al. 2019a, *PASP*, **131**, 068003
 Bellm, E. C., Kulkarni, S. R., Graham, M. J., et al. 2019b, *PASP*, **131**, 018002
 Bellm, E. C., & Sesar, B. 2016, pyraf-dbsp: Reduction pipeline for the Palomar Double Beam Spectrograph, Astrophysics Source Code Library, ascl:1602.002
 Bildsten, L., Shen, K. J., Weinberg, N. N., & Nelemans, G. 2007, *ApJL*, **662**, L95
 Bloemen, S., Marsh, T. R., Østensen, R. H., et al. 2011, *MNRAS*, **410**, 1787
 Brooks, J., Bildsten, L., Marchant, P., & Paxton, B. 2015, *ApJ*, **807**, 74
 Brooks, J., Kupfer, T., & Bildsten, L. 2017, *ApJ*, **847**, 78
 Burdge, K. B., Coughlin, M. W., Fuller, J., et al. 2019, *Natur*, **571**, 528
 Carter, D., Benn, C. R., Rutten, R. G. M., et al. 1993, *ISIS Users' Manuel* (v1.0) (Santa Cruz de La Palma: ING)
 Chambers, K. C., Magnier, E. A., Metcalfe, N., et al. 2016, arXiv:1612.05560
 Choi, J., Dotter, A., Conroy, C., et al. 2016, *ApJ*, **823**, 102
 Claret, A., & Bloemen, S. 2011, *A&A*, **529**, A75
 Clayton, G. C. 2012, *JAVSO*, **40**, 539
 Copperwheat, C. M., Marsh, T. R., Dhillon, V. S., et al. 2010, *MNRAS*, **402**, 1824
 Coughlin, M. W., Dekany, R. G., Dhev, D. A., et al. 2019, *MNRAS*, **485**, 1412
 Cummings, J. D., Kalirai, J. S., Tremblay, P. E., Ramirez-Ruiz, E., & Choi, J. 2018, *ApJ*, **866**, 21
 Dalton, G., Trager, S. C., Abrams, D. C., et al. 2012, *Proc. SPIE*, **8446**, 84460P
 de Jong, R. S., Agertz, O., Berbel, A. A., et al. 2019, *Msngr*, **175**, 3
 De, K., Kasliwal, M. M., Polin, A., et al. 2019, *ApJL*, **873**, L18
 Deng, L.-C., Newberg, H. J., Liu, C., et al. 2012, *RAA*, **12**, 735
 Dhillon, V., Dixon, S., Gamble, T., et al. 2018, *Proc. SPIE*, **10702**, 107020L
 Dhillon, V. S., Marsh, T. R., Bezawada, N., et al. 2016, *Proc. SPIE*, **9908**, 99080Y
 Dotter, A. 2016, *ApJS*, **222**, 8
 Dufton, P. L. 1972, *MNRAS*, **159**, 79
 Eggleton, P. P. 1983, *ApJ*, **268**, 368
 Fink, M., Röpkke, F. K., Hillebrandt, W., et al. 2010, *A&A*, **514**, A53
 Foreman-Mackey, D., Hogg, D. W., Lang, D., & Goodman, J. 2013, *PASP*, **125**, 306
 Gaia Collaboration, Brown, A. G. A., Vallenari, A., et al. 2018, *A&A*, **616**, A1
 Gaia Collaboration, Prusti, T., de Bruijne, J. H. J., et al. 2016, *A&A*, **595**, A1
 Geier, S., Fürst, F., Ziegerer, E., et al. 2015, *Sci*, **347**, 1126
 Geier, S., Hirsch, H., Tillich, A., et al. 2011, *A&A*, **530**, A28
 Geier, S., Marsh, T. R., Wang, B., et al. 2013, *A&A*, **554**, A54
 Geier, S., Nesslinger, S., Heber, U., et al. 2007, *A&A*, **464**, 299
 Geier, S., Raddi, R., Gentile Fusillo, N. P., & Marsh, T. R. 2019, *A&A*, **621**, A38
 Graham, M. J., Kulkarni, S. R., Bellm, E. C., et al. 2019, *PASP*, **131**, 078001
 Green, G. M., Schlafly, E. F., Zucker, C., Speagle, J. S., & Finkbeiner, D. P. 2019, arXiv:1905.02734
 Han, Z., Podsiadlowski, P., Maxted, P. F. L., & Marsh, T. R. 2003, *MNRAS*, **341**, 669
 Han, Z., Podsiadlowski, P., Maxted, P. F. L., Marsh, T. R., & Ivanova, N. 2002, *MNRAS*, **336**, 449
 Heber, U. 1986, *A&A*, **155**, 33
 Heber, U. 2009, *ARA&A*, **47**, 211
 Heber, U. 2016, *PASP*, **128**, 082001
 Hunter, J. D. 2007, *CSE*, **9**, 90
 Iben, I., Jr., & Tutukov, A. V. 1991, *ApJ*, **370**, 615
 Irrgang, A., Wilcox, B., Tucker, E., & Schiefelbein, L. 2013, *A&A*, **549**, A137
 Israel, G. L., Stella, L., Angelini, L., et al. 1997, *ApJL*, **474**, L53
 Israel, G. L., Stella, L., Angelini, L., White, N. E., & Giommi, P. 1995, *IAUC*, **6277**, 1
 Kalirai, J. S., Marigo, P., & Tremblay, P.-E. 2014, *ApJ*, **782**, 17
 King, A. R., & Ritter, H. 1998, *MNRAS*, **293**, L42
 Koen, C., Orosz, J. A., & Wade, R. A. 1998, *MNRAS*, **300**, 695
 Kollmeier, J. A., Zasowski, G., Rix, H.-W., et al. 2017, arXiv:1711.03234
 Kudritzki, R. P., & Simon, K. P. 1978, *A&A*, **70**, 653

- Kupfer, T., Geier, S., Heber, U., et al. 2015, *A&A*, 576, A44
- Kupfer, T., Korol, V., Shah, S., et al. 2018, *MNRAS*, 480, 302
- Kupfer, T., Ramsay, G., van Roestel, J., et al. 2017a, *ApJ*, 851, 28
- Kupfer, T., van Roestel, J., Brooks, J., et al. 2017b, *ApJ*, 835, 131
- Livne, E. 1990, *ApJL*, 354, L53
- Livne, E., & Arnett, D. 1995, *ApJ*, 452, 62
- Loeb, A., & Gaudi, B. S. 2003, *ApJL*, 588, L117
- Macfarlane, S. A., Toma, R., Ramsay, G., et al. 2015, *MNRAS*, 454, 507
- Macfarlane, S. A., Woudt, P. A., Groot, P. J., et al. 2017, *MNRAS*, 465, 434
- Marsh, T. R., Nelemans, G., & Steeghs, D. 2004, *MNRAS*, 350, 113
- Masci, F. J., Laher, R. R., Rusholme, B., et al. 2019, *PASP*, 131, 018003
- Maxted, P. F. L., Heber, U., Marsh, T. R., & North, R. C. 2001, *MNRAS*, 326, 1391
- Maxted, P. F. L., Marsh, T. R., & North, R. C. 2000, *MNRAS*, 317, L41
- McCarthy, J. K., Cohen, J. G., Butcher, B., et al. 1998, *Proc. SPIE*, 3355, 81
- Mereghetti, S., & La Palombara, N. 2016, *AdSpR*, 58, 809
- Mereghetti, S., La Palombara, N., Tiengo, A., et al. 2011, *ApJ*, 737, 51
- Mereghetti, S., La Palombara, N., Tiengo, A., et al. 2013, *A&A*, 553, A46
- Mereghetti, S., Tiengo, A., Esposito, P., et al. 2009, *Sci*, 325, 1222
- Morris, S. L. 1985, *ApJ*, 295, 143
- Napiwotzki, R., Karl, C. A., Lisker, T., et al. 2004, *Ap&SS*, 291, 321
- Nelemans, G. 2010, *Ap&SS*, 329, 25
- Nomoto, K. 1982, *ApJ*, 253, 798
- Nomoto, K., Saio, H., Kato, M., & Hachisu, I. 2007, *ApJ*, 663, 1269
- Odenkirchen, M., & Brosche, P. 1992, *AN*, 313, 69
- Oke, J. B., & Gunn, J. E. 1982, *PASP*, 94, 586
- Oliphant, T. E. 2015, *Guide to NumPy* (2nd ed.; USA: CreateSpace Independent Publishing Platform)
- Orosz, J. A., & Wade, R. A. 1999, *MNRAS*, 310, 773
- Patterson, J., & Raymond, J. C. 1985, *ApJ*, 292, 535
- Pauli, E.-M., Napiwotzki, R., Heber, U., Altmann, M., & Odenkirchen, M. 2006, *A&A*, 447, 173
- Paxton, B., Bildsten, L., Dotter, A., et al. 2011, *ApJS*, 192, 3
- Paxton, B., Cantiello, M., Arras, P., et al. 2013, *ApJS*, 208, 4
- Paxton, B., Marchant, P., Schwab, J., et al. 2015, *ApJS*, 220, 15
- Paxton, B., Schwab, J., Bauer, E. B., et al. 2018, *ApJS*, 234, 34
- Paxton, B., Smolec, R., Schwab, J., et al. 2019, *ApJS*, 243, 10
- Perets, H. B., Zenati, Y., Toonen, S., & Bobrick, A. 2019, arXiv:1910.07532
- Perley, D. A. 2019, *PASP*, 131, 1002
- Piersanti, L., Tornambé, A., & Yungelson, L. R. 2014, *MNRAS*, 445, 3239
- Polin, A., Nugent, P., & Kasen, D. 2019, *ApJ*, 873, 84
- Pringle, J. E., & Savonije, G. J. 1979, *MNRAS*, 187, 777
- Ramsay, G., Kennedy, M., Hakala, P., & Jeffery, C. S. 2019, *ATel*, 13048, 1
- Ratzloff, J. K., Barlow, B. N., Kupfer, T., et al. 2019, *ApJ*, 883, 51
- Ritter, H. 1988, *A&A*, 202, 93
- Rivera Sandoval, L. E., Maccarone, T., & Murawski, G. 2019, *ATel*, 12847, 1
- Saio, H. 2008, in *ASP Conf. Ser.* 391, *Hydrogen-Deficient Stars*, ed. A. Werner & T. Rauch (San Francisco, CA: ASP), 69
- Savonije, G. J., de Kool, M., & van den Heuvel, E. P. J. 1986, *A&A*, 155, 51
- Scargle, J. D. 1982, *ApJ*, 263, 835
- Shen, K. J., & Bildsten, L. 2014, *ApJ*, 785, 61
- Stroeer, A., Heber, U., Lisker, T., et al. 2007, *A&A*, 462, 269
- Thackeray, A. D. 1970, *MNRAS*, 150, 215
- Toma, R., Ramsay, G., Macfarlane, S., et al. 2016, *MNRAS*, 463, 1099
- Tutukov, A. V., & Fedorova, A. V. 1989, *SvA*, 33, 606
- Tutukov, A. V., & Yungelson, L. R. 1990, *SvA*, 34, 57
- Vanderplas, J. 2015, *gatspy: General Tools for Astronomical Time Series in Python*, v0.3.0, Zenodo, doi:10.5281/zenodo.14833
- VanderPlas, J. T., & Ivezić, v. 2015, *ApJ*, 812, 18
- Vennes, S., Kawka, A., O'Toole, S. J., Németh, P., & Burton, D. 2012, *ApJL*, 759, L25
- Wang, B. 2018, *RAA*, 18, 049
- Wang, B., & Han, Z. 2012, *NewAR*, 56, 122
- Wheatley, P. J., Mauche, C. W., & Mattei, J. A. 2003, *MNRAS*, 345, 49
- Wolf, W. M., Bildsten, L., Brooks, J., & Paxton, B. 2013, *ApJ*, 777, 136
- Woosley, S. E., & Kasen, D. 2011, *ApJ*, 734, 38
- Yungelson, L. R. 2008, *AstL*, 34, 620
- Zenati, Y., Toonen, S., & Perets, H. B. 2019, *MNRAS*, 482, 1135